Reservoir Characterization Using Seismic Reflectivity and Attributes

by

Abdulrahman Mohammad Saleh Al-Moqbel

Submitted to the Department of Earth, Atmospheric, and Planetary Sciences
in partial fulfillment of the requirements for the degree of

Master of Science in Geophysics

at the

MASSACHUSETTS INSTITUTE OF TECHNOLOGY

June 7, 2002

Author .....
Department of Earth, Atmospheric, and Planetary Sciences
May 11, 2002

Certified by .....
Professor M. Nafi Toksöz
Professor of Geophysics
Thesis Supervisor

Accepted by .....
Ronald G. Prinn
Chairman, Department of Earth, Atmospheric and Planetary Sciences

Reservoir Characterization Using Seismic Reflectivity and Attributes

by

Abdulrahman Mohammad Saleh Al-Moqbel

Submitted to the Department of Earth, Atmospheric, and Planetary Sciences
on May 18, 2002, in partial fulfillment of the
requirements for the degree of
Master of Science in Geophysics

Abstract

The primary objective of this thesis is to obtain reservoir properties, such as porosity from surface seismic data complemented by available well logs. To accomplish this a two-step procedure is followed. First, reflectivity and acoustic impedance profiles are obtained from the inversion of post-stack seismic data. Second, a multi-attribute analysis, calibrated using well logs, is used to obtain porosity.

This procedure is applied to a 40x40 sq. km field data set from the eastern region of Saudi Arabia. The 3-D seismic data are of good quality. Twenty-one wells have a good suite of logs. The analysis is focused on the reflections from the reservoir.

The outcome of the thesis is an improved subsurface image of the seismic data, a porosity prediction for the reservoir, and a reservoir quality map obtained by similarity analysis using one of the wells as reference.

Thesis Supervisor: Professor Nafi Toksöz
Title: Professor of Geophysics

Acknowledgments

I owe a debt of gratitude to some very special people. Immense appreciation goes to my academic advisor at MIT, Prof. Nafi Toksöz who accepted me for the master's program at MIT, helped me throughout my stay in Cambridge, and also made this moment real. Prof. Nafi, like Dr. Dan Burns, gave continuous help and support, constructive recommendations, unlimited kindness and understanding. I thank them for their moral support and understanding in the critical time, and for being there for me when I needed talking to them.

My undergraduate advisor, Dr. Kurt Kramer, also deserves special thanks for his lasting help and support, and making my graduate study at MIT possible. Dr. Kramer, along with Saleh Al-Maglooth and Martin Dickens, wrote the required recommendation letters for my application to MIT, which I greatly appreciated.

I am thankful to my Saudi government and the Saudi Arabian Oil Company (Saudi Aramco Company) for funding my graduate education throughout my stay in the United States.

I gratefully acknowledge support from vice president of Saudi Aramco Company's Exploration Organization, Mahmood Abdulbagi; manager of Exploration Department, Abdullah Al-Nuaim; division heads, Ali Al-Hawwaj and Saleh Al-Maglooth; my team leaders, Martin Dickens, Bob Jonson, Abdulkareem Al-Qahtani, Greg Douglas, and Khalid Al-Mashooq; and my other colleagues and friends at Saudi Aramco Company. I would also thank here all those who nominated me for admission to the master's degree program and express my very special thanks to those who continuously pass on their greetings and encouragement.

I thank everyone in the Earth Resources Laboratory (ERL) at MIT, particularly Sudipta Sarkar, Samantha Grandi, Sadi Kulili, Youshun Sun, Mary Krasovec, Vic-

toria Briggs, Roberta Bennett-Calorio, Rama Rao, Bill Rodi, Zhenya Zhu, Vernon Cormier, David Harkrider, Rob Reilinger, Ted Madden, and Dale Morgan. Special thanks to Jonathan Kane, Abdulfattah Al-Dajani, Darrell Coles, Xiaojun Huang, Edmund Sze, John Sogade, Sue Turbak, and Liz Henderson. I am grateful to them for their help, and kindness.

I thank Joe Hankins in Lindgren library for his continuous help. Also, Linda Meinke and Scott Blomqist are thanked for their effective support whenever hardware or software problems occur. Judith Stitt's help was also much appreciated.

I thank my current Aramco advisor, Brad Brumfield, in the United States and my former advisor in Saudi Arabia, Arny Rivett, for their fruitful visits and warm encouragement. I thank my new advisor, Ronald Clark, for his help, and understanding.

I thank Muhammad Saggaf and Hafiz Al-Shammari for their feedback and comments. I thank my friends here in Cambridge, Abdulaziz Al-Nuaim, Hamad Al-Saleh, Riyadh Muawad, and Dari Al-Wazan, for making our stay in Cambridge more fun, exciting, and as memorable as possible. I also thank my friend Jeff Snyder for his encouragement and kindness.

I also have appreciated the help, support, and encouragement of my cousins, Mansour Al-Moqbel and Abdulrahman Al-Rashid; and my friend Dr. Thaiyer Al-Dulaimi and his family. My special regards and thanks go to them.

I thank my parents, brothers, and sisters for their continuous moral and spiritual support, as well as for their unlimited help and support in every passing moment. They made this moment a real one. I thank my brother, Abdulaziz, for his invaluable help and support.

I thank my friends, relatives, and everyone who taught me, helped me, or supported me throughout my life.

I am very grateful to my god. I express all the thanks and glory to Allah for the care, guidance, love, and mercy to make this event part of my destiny.

I dedicate my thesis to my parents, brothers, sisters, and the loved ones who I lost throughout the years.

List of Figures

Contents

Chapter 1

INTRODUCTION

1.1 Introduction

In petroleum exploration, the first step towards a successful hydrocarbon discovery is a good subsurface image of seismic data. Seismic data is first processed to increase its signal-to-noise ratio and interpreted to determine subsurface geology. Seismic data is the output of a convolution operation between the earth reflectivity and a source wavelet. The convolution operation causes a major problem in the seismic data. It produces a band-limited trace, whose bandwidth is determined by the seismic wavelet. In other words, most of the low and high frequency components of the reflectivity are lost. Inverting the seismic data to the reflectivity is tempting since it would improve the subsurface image quality and would provide a physical parameter (reflectivity) that is directly related to formation properties.

Reservoir characterization plays an essential role in the exploration and development of a given field. It contributes to the prediction of the properties as well as to the economic potential of the field. In general, a reservoir study can be classified to four different scales: microscopic, mesoscopic, macroscopic, and megascopic. Predicting a reservoir characteristic of a filed exactly is impossible due to the data resolution problems. The two main types of data are seismic data and well data. The former provides larger coverage but with a low resolution (approximately 30 m),

while the latter provides a higher resolution (approximately 10 cm) but at a few, scattered locations. Large-scale (megascopic) prediction of the reservoir properties, such as porosity, for a given field is an important objective. Achieving this objective starts with integrating the seismic data with the well data.

Seismic attributes analysis can play a significant role in the reservoir's property prediction by revealing information that may not be evident in the standard amplitude data. A suite of properties of seismic trace (such as amplitude, phase, and frequency) can be crossplotted with the well logs to find the relation between the two types of data. The attributes selected on the basis of correlation with the petrophysical property can be effective in estimating reservoir properties away from the wells.

Many seismic attributes have been used in reservoir characterization. Multi-attributes analysis can be either deterministic or statistical in nature. A similarity map is an example of statistical analysis. It uses one of the wells (e.g., a high producing well) as a reference location and tries to map the field based on the similarity to the reference well. Deterministic use of attributes requires the derivation of properties from each seismic trace by formal inversion. In this thesis we will use both approaches.

1.2 Objectives

The following are the main objectives of the thesis. The first is to invert the original seismic data to the reflectivity data for a better subsurface image using a joint kriging-deconvolution technique. The second objective is to invert the reflectivity cube to the acoustic impedance cube by integration using the least-squares method for further reservoir study. The third is to use an attribute analysis to extract further from the data, and to produce a reservoir porosity map. The final objective is to test the effectiveness of the method by correlation of the seismically-derived porosity, and measured porosity at the wells.

1.3 Outline of the Thesis

The thesis consists of six chapters. The first chapter contains the main objectives of the thesis. The second chapter describes the field area, the geologic setting, the reservoir, data types, and the number of wells. The third chapter is devoted to analysis and inversion of seismic data to obtain reflectivity and acoustic impedance. The fourth chapter covers the seismic attributes of the applications of multi-attributes analysis to our field data. The fifth chapter evaluates the performance of attribute analysis by correlation with well data. The sixth chapter contains the conclusions. Figure 1-1 is a flowchart showing the general processes and outcomes of this paper.

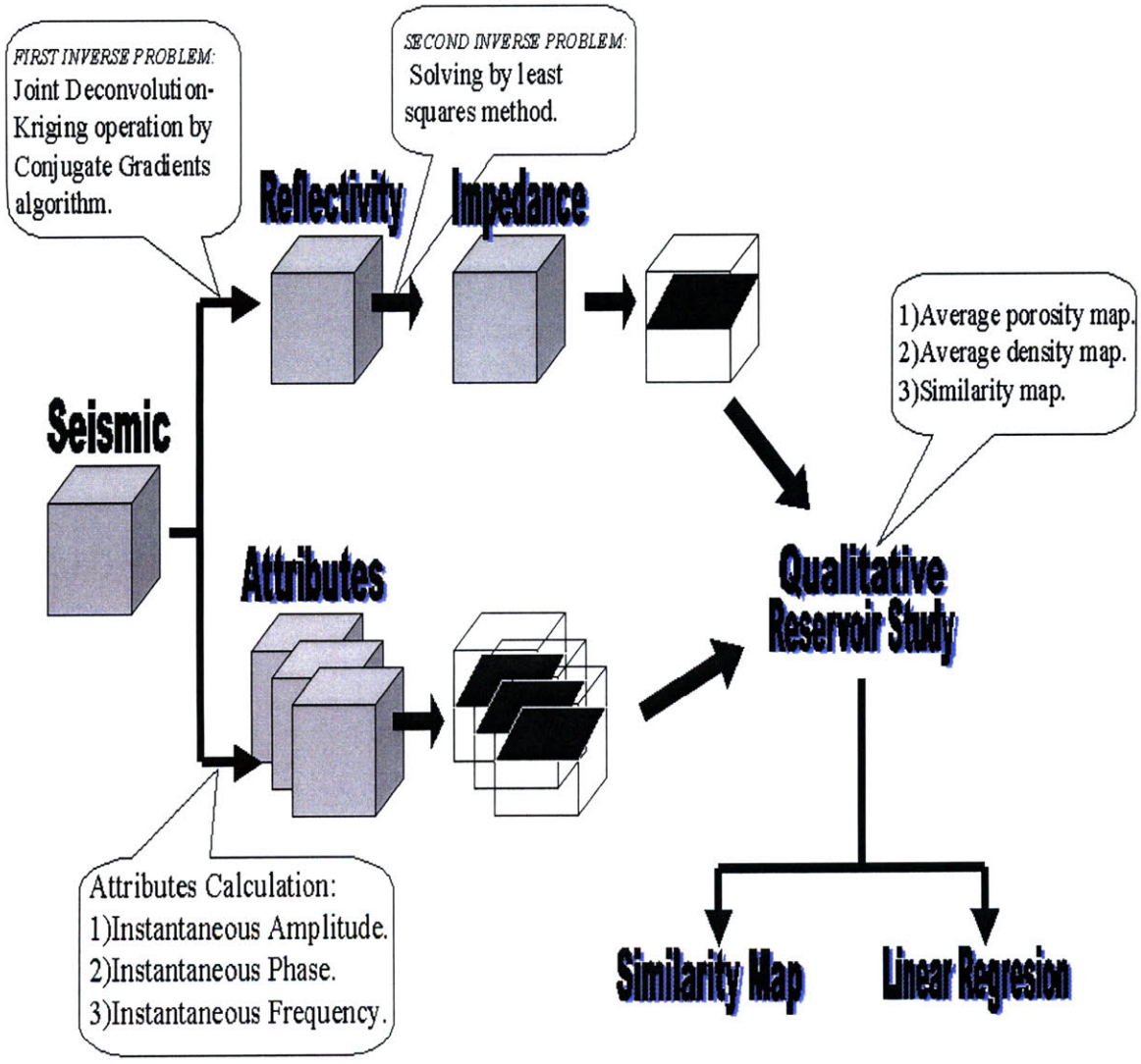

Figure 1-1: Flowchart of the general processes and outcomes of the thesis.

Chapter 2

FIELD DESCRIPTION

2.1 Field and Data

The field which is located in the eastern region of Saudi Arabia (Figure 2-1), covers (40x40 sq.km) area. Three-dimesional seismic volume and well data were used for this study. There are 21 wells within the area, which can be classified as production wells, injection wells, and observation wells. The production wells range from high to low producing wells. The second type of data, 3D seismic data, is Rap-Dmo-Migrated poststack volume. It is limited from 700 (ms) to 1500 (ms) in the time section (Z-direction). There are (401) inlines in the east-west direction (X-direction) and (401) cross-lines in the north-south direction (Y-direction). The data quality of the 3D cube is excellent on the top-reservoir level (Figure 2-2 and 2-3).

2.2 Geologic Background

2.2.1 Stratigraphic Section

The stratigraphic section is made up of a series of a carbonate and anhydrite sequences. It contains the main elements required for favorable hydrocarbons occurrence; source, reservoir, trap, and seal rocks. The formation consists of four geographically widespread carbonate-evaporite cycles or members (Cantrell and Hagerty, 1999)

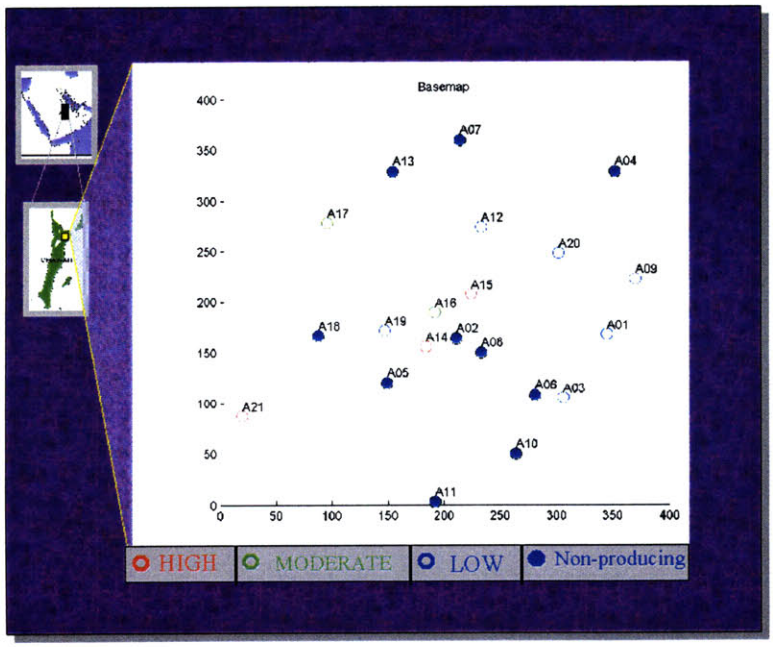

Figure 2-1: Basemap of the (40x40 sq.km) study area in eastern region of Saudi Arabia. It shows the wells' locations and classification. There are 401 (E-W) inlines and 401 (N-S) crosslines

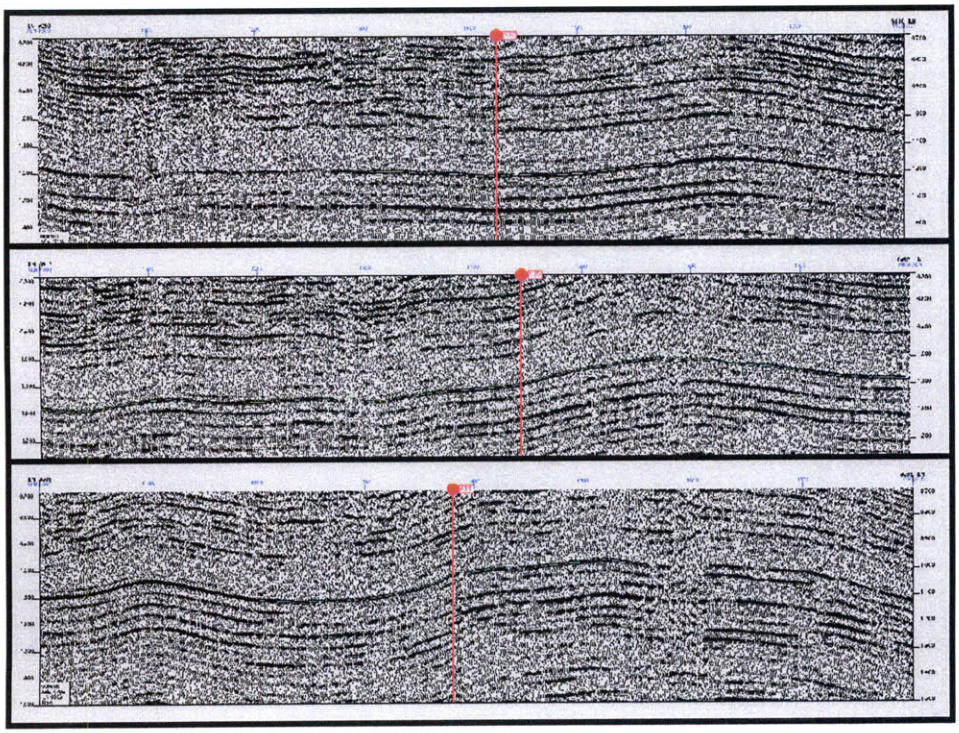

Figure 2-2: E-W inlines through A07, A15, and A11 from top to bottom, respectively.

(Figure 2-4). The lowermost carbonate is the oldest and the one relevent to this study. It is overlain by anhydrite that acts as a seal for hydrocarbons. The base of the reservoir is defined by a gradational change from low energy mudstones(bottom) to high energy grainstones(top). Reservoir quality generally improves from the base to the top. In general, the structures of the area have a NNW-SSW striking anticlinal trends and show low dips. Structural growth took place throughout the Cretaceous period. In general, the area shows northeastward tilting.

2.2.2 Paleogeographic Setting

The formation was deposited on a shallow marine(carbonate) shelf 150 million years ago when a major seaway separated the African and Eurasian crustal plates before the opening of the Atlantic ocean.

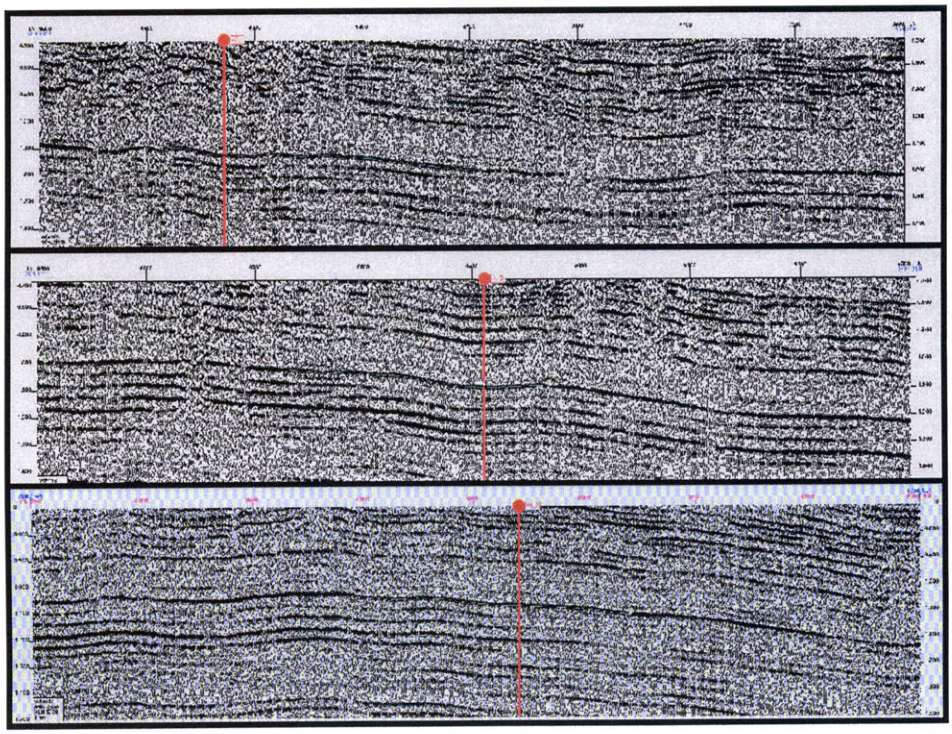

Figure 2-3: N-S crosslines through A21, A15, and A09 from top to bottom, respectively.

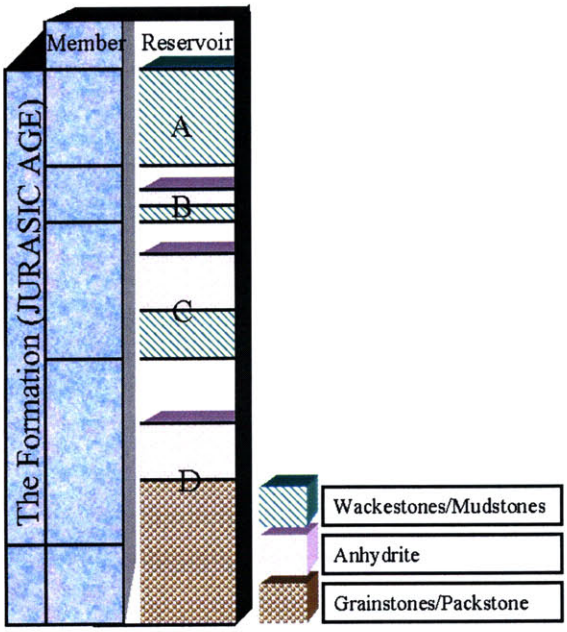

Figure 2-4: Generalized Stratigraphic Column. Reservoir of interest is a carbonate unit on top of D

2.2.3 Lithology

The main lithology of the reservoir is limestone and dolomite. The dolomite makes up 15-20 percent of the reservoir. It formed during diagenesis by the alternation of pre-existing limestone. The most productive facies of the reservoir is made up of calcarious sand or calcarenite. All hydrocarbon occurrences within the reservoir appear to be entirely structurally controlled. However, stratigraphic hydrocarbon accumulations are possible. Dolomitization occures as thin beds in the middle of the reservoir. Porous crystal fabrics make up a significant component within certain dolomitized intervals in the formation (Meyer and Cantrell, 2000). The upper and lower parts of the reservoir contain minor amounts of dolomite. Sometimes vertical fractures occur within dolomite. Most of the fractures are filled with calcite, dolomite or anhydrite cement. These fractures affect local permeability.

Chapter 3

DATA ANALYSIS AND INVERSION

3.1 Data Analysis

Two main types of data were available for this study: 3D-seismic and well data. The 3D seismic data was first uploaded into Geoframe application (IESX) to tie the well data to the seismic. The top of the reservoir was extended from the well data to the seismic cube and a seismic horizon was picked over most of the seismic volume. Next, the surface of the picked horizon was used to flatten the cube. The volume was flattened 224(ms) above the picked surface in a step needed for the calibration between seismic data and well data in the inversion operations. Working with the flattened volume was easier than the unflattened because the reference horizon was fixed over the vertical time axis. The location of the reference horizon was very well-known everywhere in the cube, at the 57'th time sample. The dimensions of the flattened cube were 201 samples in Z-direction (the vertical time axis), 401 crosslines in Y-direction (N-S), and 401 inlines in X-direction (E-W).

The second dataset was a group of twenty one wells scattered over the area. Each of the wells had different types of logs. Sonic and density logs were available for every well. The velocity log and density log were used to generate the impedance and reflectivity logs as a function of depth. The velocity, density, impedance, and

reflectivity logs for one of the wells are shown in Figures 3-1 and 3-2.

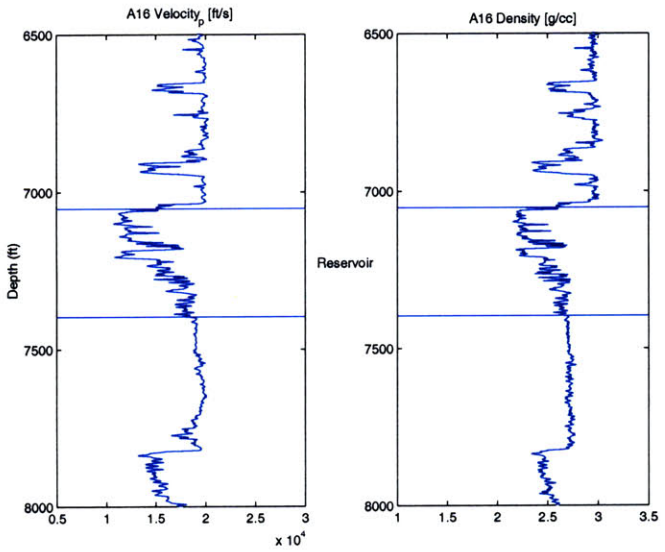

Figure 3-1: Velocity and density logs for well A16.

There is much information which can be used to constrain seismic inversions for reservoir description (Castagna, 1994). The reflectivity logs of the wells were needed as reference step to obtain the reflectivity cube. Consequently, they were converted from depth to time and then calibrated with the seismic cube (Figure 3-3). The conversion from depth to time was a two-step process; it was converted to irregular time samples then resampled as a regular seismic time sample (Figure 3-4). This Reflectivity data was used to obtain the acoustic impedance. The integrated acoustic impedance logs at the well locations were derived then calibrated with the seismic before starting the second inversion operation (Figure 3-5).

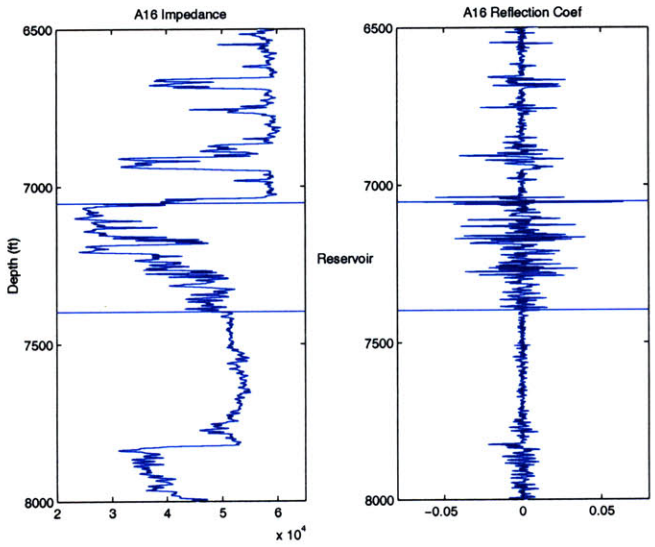

Figure 3-2: Impedance and reflectivity logs for well A16.

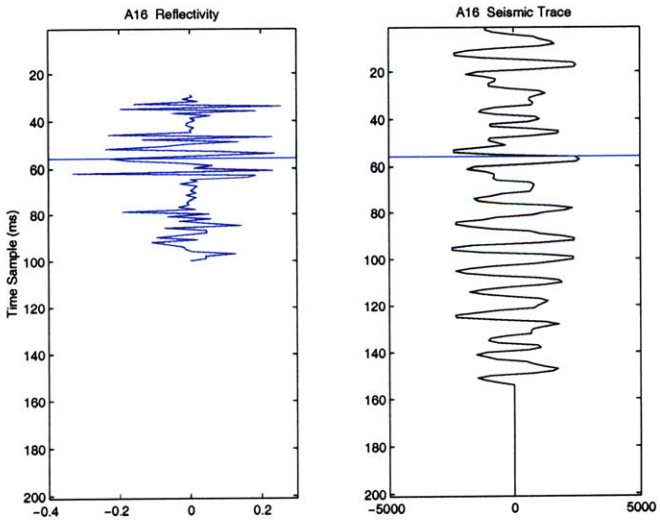

Figure 3-3: Calibrated reflectivity and seismic trace at well A16.

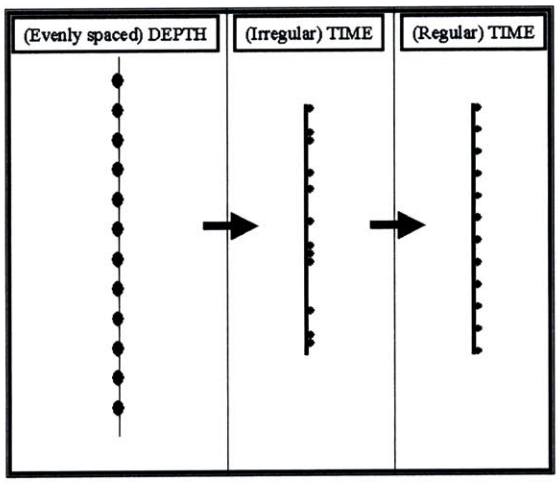

Figure 3-4: Depth to time conversion steps.

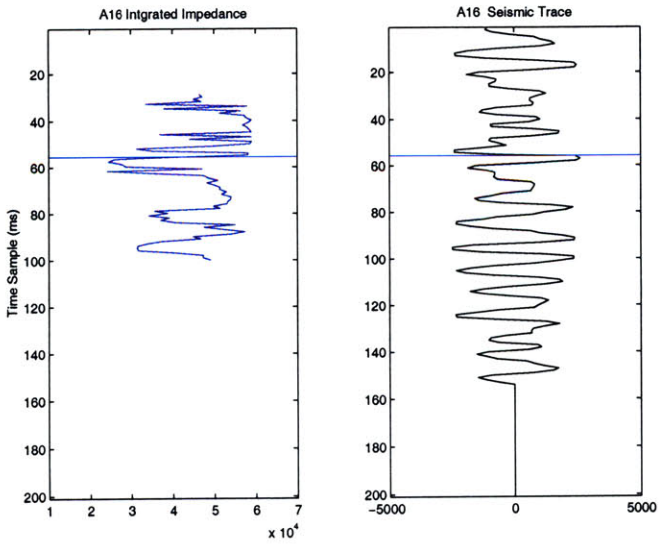

Figure 3-5: Calibrated impedance and seismic trace at well A16.

3.2 Inversion of Seismic Data

Seismic inversion can be defined as the process of mapping some geophysical properties of the subsurface from surface seismic data. Any inversion process suffers from the uncertainty (nonuniqueness) associated with the frequency components outside the dominant signal bandwidth (Yilmaz, 2001). When signal-to-noise ratio is low, the inversion results could be questionable for the low and high frequencies of the spectrum. Usually the inversion process is constrained by well data.

A seismic trace is the output of a forward modeling of three main components: the earth reflectivity, the seismic wavelet, and noise. A seismic trace can be expressed by the following convolutional model:

$$s(t) = w(t) * r(t) + n(t), \tag{3.1}$$

where

$$\begin{aligned} s(t) &= \text{seismic trace,} \\ r(t) &= \text{earth reflectivity,} \\ w(t) &= \text{a seismic wavelet,} \\ n(t) &= \text{noise.} \end{aligned}$$

The resolution of the seismic trace is much lower than that of the real earth reflectivity. Based on the processing stage of the data, seismic inversion can be classified either prestack and poststack inversion. The seismic data available for this study is poststack.

Inverse problems can be solved in different ways; the least squares method is one of the most robust types. It can handle linear and non-linear problems. Inverting seismic data to acquire reflectivity is a linear problem, while inverting reflectivity to acquire acoustic impedance is a non-linear problem.

Two main inversion operations were done in the following two sections: Reflection Coefficient (R) and Acoustic Impedance (I). The conjugate gradients algorithm was used in the first operation. This algorithm guarantees that the error between the seismic trace and the reflectivity trace is reduced at each iteration (Smith and Scales, 1997). The 3D seismic data was constrained by the well data to give a better result. Well data has a higher resolution than does seismic data and reveals more accurate information about geophysical properties at well locations. On the other hand, 3D seismic data provides a larger data coverage, but with much lower resolution. The first step was to invert for the reflectivity and use the result as an input for the second inversion operation for obtaining the acoustic impedance.

3.2.1 Reflection Coefficient (R)

Reflection coefficient (R) is defined as the ratio of the amplitude of the reflected wave to the incident wave (Aki and Richards, 1980). For a normal incident wave, R can be expressed as:

$$R = \frac{I_2 - I_1}{I_2 + I_1}, \tag{3.2}$$

where

R = reflection coefficient.

I_1 = acoustic impedance of the upper layer.

I_2 = acoustic impedance of the lower layer.

At non-normal incidence, R is defined as a ratio of amplitude that depends on other parameters such as shear velocities, and is described as a function of incident angle by the Zoeppritz equations. A negative reflection coefficient implies phase inversion, that a compression is reflected as a rarefaction (Sheriff, 1992).

A seismic trace results from the convolution operation between the earth reflectivity and a band-limited seismic pulse. A comparison of the resolution of the seismic trace with that of the reflectivity shows a loss of resolution in the seismic trace. The bandlimited seismic trace is produced by the convolution operation. An attempt to recover this resolution is made by obtaining the reflectivity through a deconvolution operation, which is an inverse problem (Robinson and Silvia, 1978). Constraining this operation with the well data should give a better result which honors the well data. Acquiring the reflectivity by solving a joint inverse problem, deconvolving the seismic and kriging the well data, is an optimal way to get a better subsurface image (Kane, 2000). In most exploration and reservoir seismic surveys, the main objectives are to correctly image the structure in time and depth, and to correctly characterize the amplitudes of the reflections in both the stacked and prestacked domains (Pennington, 2001).

Starting with the well data, velocity and density logs were used at every well location to calculate the reflectivity log as a function of depth. These reflectivity logs were then converted from depth to two-way traveltime in two steps: irregular time, then regular time. Prior knowledge of the reservoir depth at a well's location helped in calibrating the well data to the seismic data. There is a good correlation between the seismic trace and the derived reflectivity (3-6. The amplitude spectrum for both the seismic trace and the reflectivity is shown for well A02 in Figure 3-7. The well reflectivity logs and the 3D seismic data were simultaneously kriged and deconvolved to obtain the reflectivity in the form of a linear inverse problem following the approach given by Kane (2000 and 2002). This process is described in Appendix A. The wavelet used in this study is shown in Figure 3-8.

Three different equations were set to represent the relationship between the reflectivity and seismic data, well data, and a smoothness operator:

$$s = Hr + n_H \ , \tag{3.3}$$

where

$$
\begin{aligned}
s &= \text{seismic traces (from 3D seismic data)} \\
r &= \text{reflectivity traces to be calculated} \\
H &= \text{convolution operator} \\
n_H &= \text{white noise from the convolution operation}
\end{aligned} \tag{3.4}
$$

H is a block diagonal matrix. Each diagonal block is a Toeplitz matrix that convolves each reflectivity trace with a seismic wavelet. In other words, if the trace is (201) time samples, then H_{block1} is the first block matrix of size (201x201) where each row is the wavelet shifted by one sample from the previous row. $H_{block(1)} = H_{block(2)} = ... = H_{block(N)}$, where (N) is the total number of traces (401x401). Therefore, there are (N) blocks on the diagonal of (H). n_H is a random vector that represents the noise in the

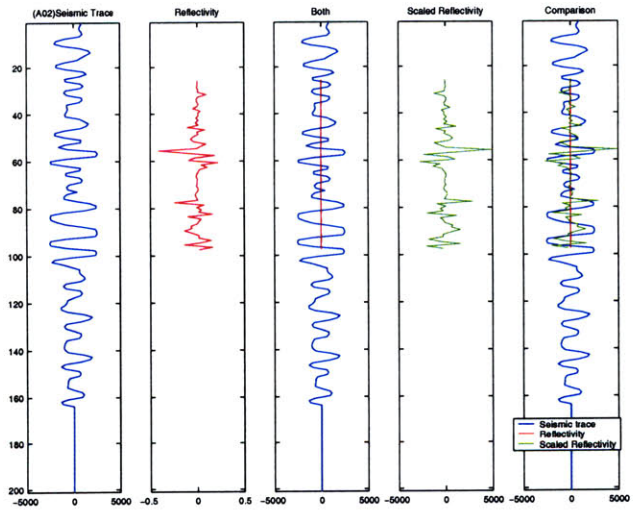

Figure 3-6: A seismic trace and its derived reflectivity. The scaled reflectivity is the is the well reflectivity multiplied by -12000 to match the seismic trace.

seismic data as well as the inherent inaccuracy of H. It is assumed to be stationary white noise with variance ${\sigma_H}^2$ and uncorrelated with r. $n_H = \sigma_H n_H{}'$, where $n_H{}'$ is the noise with a unit variance. Another way to think of white noise in a matrix representation is that the covariance of the matrix equals the variance multiplied by the identity ($C = \sigma I$). The covariance of any vector (n_H) is the expected value of

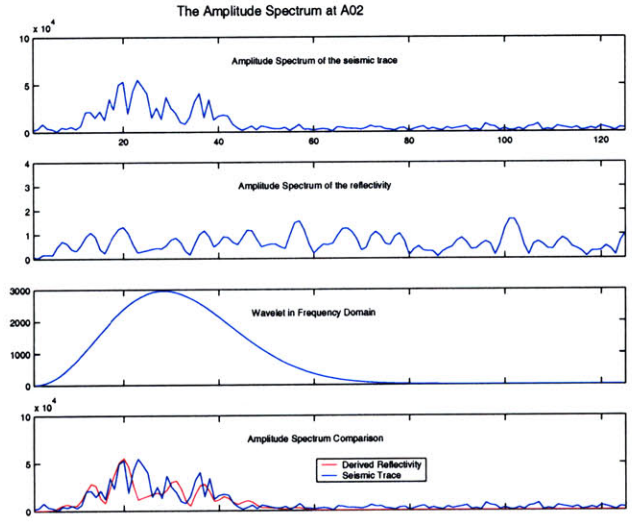

Figure 3-7: The amplitude spectrum of the seismic trace and the derived reflectivity at A02.

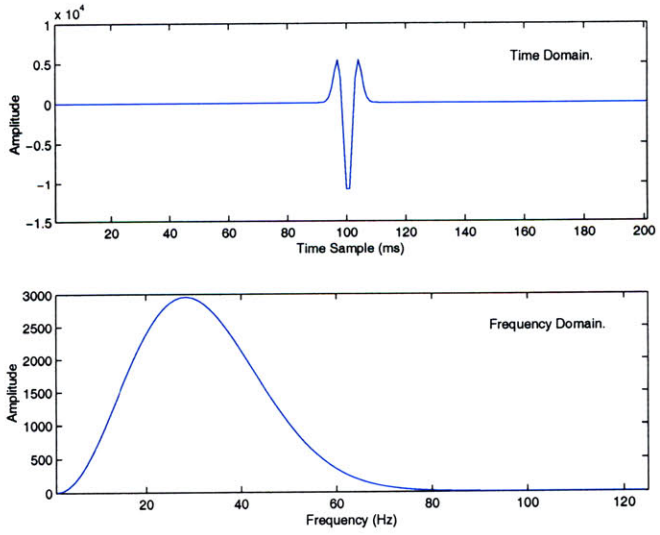

Figure 3-8: The source wavelet in time and frequency domains.

that vector multiplied by its transpose (C=E(n_H $n_H{}^T$). H^T represents correlation, while H represents convolution.

For $i \neq j$ (off diagonal), $C = 0 \Rightarrow$ (uncorrelated).

For $i = j$ (diagonal), $C = \sigma I \Rightarrow$ (white noise).

The 'stationary' term means that the values on the diagonal are the same and with equal variance.

The second equation is the kriging (interpolation) equation:

$$d = Pr + n_P \,, \tag{3.5}$$

where

d = observed reflectivity traces (from well data)

P = kriging operator

n_P = white noise from the kriging operation

P is a rectangular matrix made up of a subset of the rows of the identity matrix. The identity matrices coincide with the traces at the well locations. The identity matrices differ in size depending on the length of the well reflectivity in time samples. P "picks" the observed data out of the reflectivity field r. n_P is a random white noise with variance $\sigma_P{}^2$ and uncorrelated with r. $n_P = \sigma_P n_P{}'$, where $n_P{}'$ has a unit variance.

The third equation is a measure of the field smoothness from the kriging operation:

$$Lr = n_L \ , \tag{3.6}$$

where

L = differencing operator,

n_L = white noise with variance ${\sigma_L}^2$.

L is introduced to account for the smoothness effect in the kriging operation. It has a relationship to the covarince matrix that is widely used in most geostatistical operations ($L^T L^{-1}$ = the covariance matrix). For a given trace, differencing the trace will roughen it while integrating the trace will smooth it. Estimating the amount of smoothness by the kriging operation on the reflectivity field can be achieved by minimizing the difference operator acting on that field.

These three equations (3.3 to 3.6) are combined into one linear equation:

$$(\lambda_1 H^T H + P^T P + \lambda_2 L^T L)r = \lambda_1 H^T s + P^T d \tag{3.7}$$

The mathematical derivation to equation 3.7 is shown in Appendix A.

The analysis steps described above were applied to the data. Figure (3-9) shows a sliced 3D image from the original seismic cube. Figures 3-10, 3-11, 3-12, and 3-13 show the results of a kriging operation, a deconvolution operation without any damping applied, a deconvolution operation with damping, and the joint deconvolution-kriging operation, respectively. Figures 3-14, 3-15, and 3-16 show the examples of comparison of the reflectivity and the seismic data for three in-line sections. Figures 3-17, 3-18, and 3-17 are the comparison for three cross-line sections.

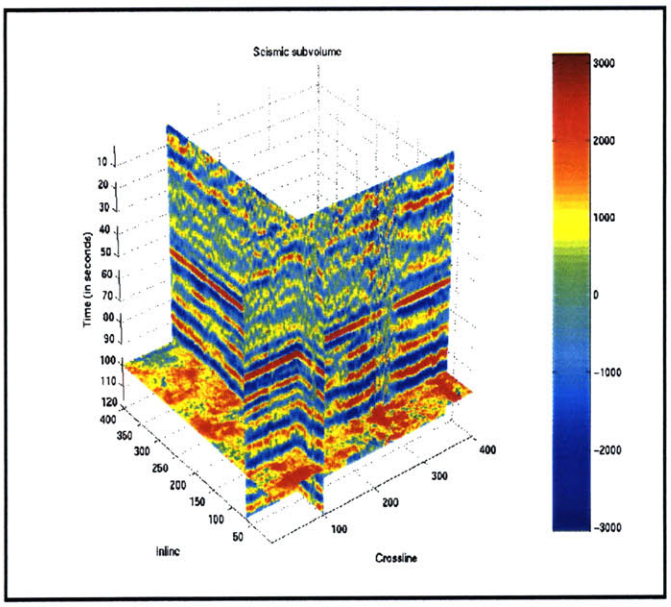

Figure 3-9: Original seismic data.

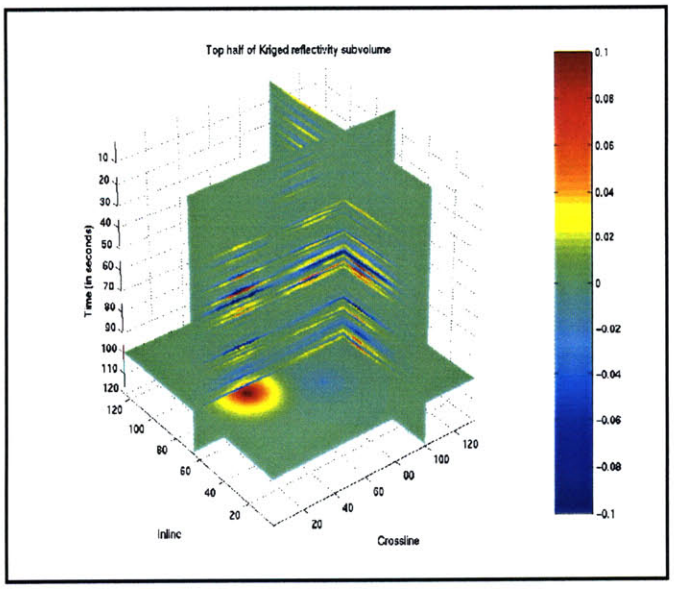

Figure 3-10: Derived reflectivity from well data by kriging operation.

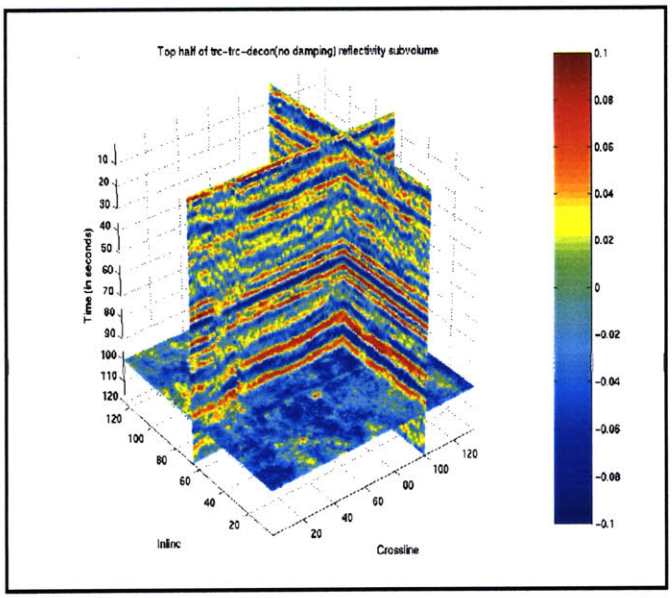

Figure 3-11: Derived reflectivity by deconvolution operation without damping.

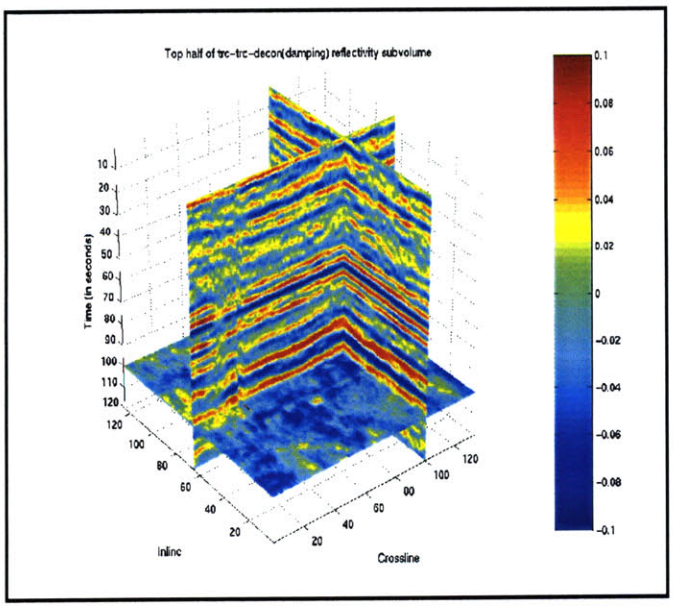

Figure 3-12: Derived reflectivity by deconvolution operation with damping.

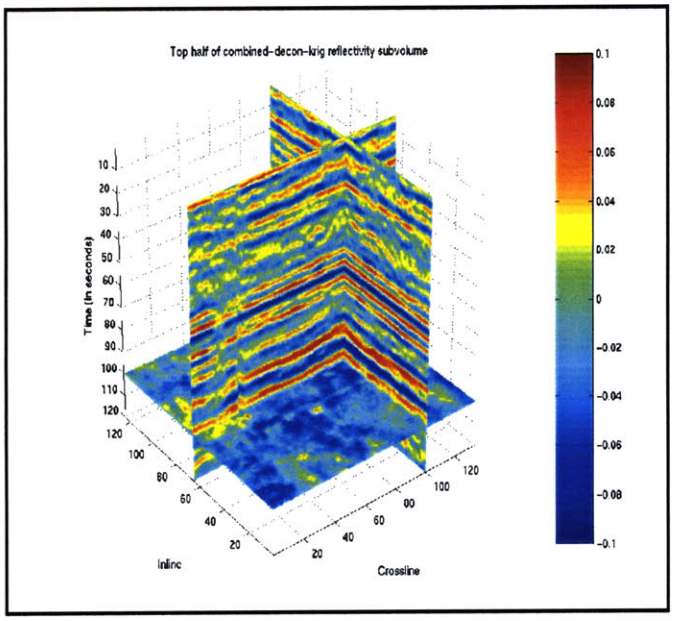

Figure 3-13: Derived reflectivity by joint deconvolution-kriging operation.

3.2.2 Acoustic Impedance (I)

The acoustic impedance, I, of a material is defined as the product of density, ρ, and acoustic velocity, V.

$$I = \rho V, \tag{3.8}$$

After the the reflectivity cube was acquired from the first inversion operation, and after the impedance logs at the wells' locations were converted to time then calibrated with the seismic cube as shown in Figures 3-20 , 3-21 , and 3-22, the second operation was started to obtain the acoustic impedance cube. The inversion was possible after linearizing the inverse problem.

The reflection coefficient equation at normal incidence is given by Equation 3.8 :

$$R(t) = \frac{I_2 - I_1}{I_2 + I_1}.$$

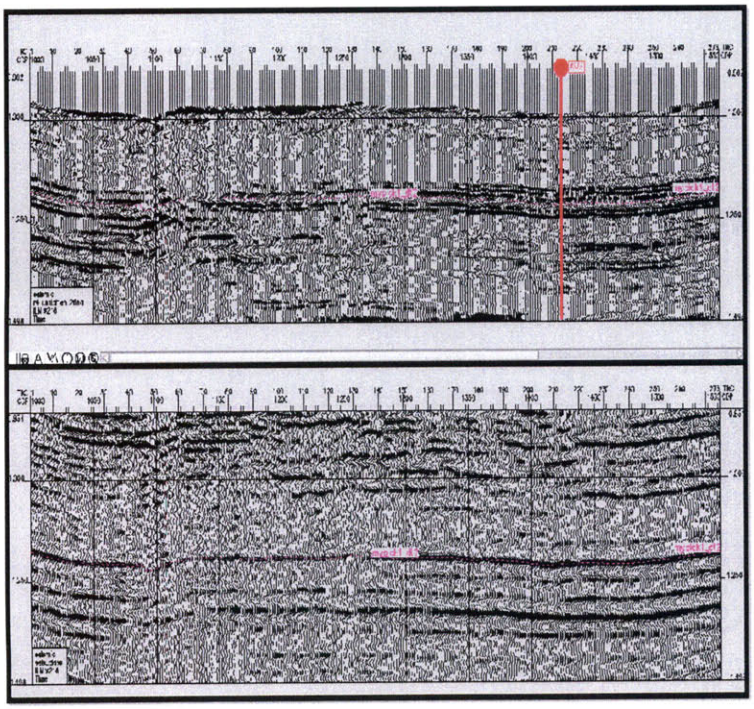

Figure 3-14: Inline through A07: derived reflectivity [Top] , and original seismic section [Bottom].

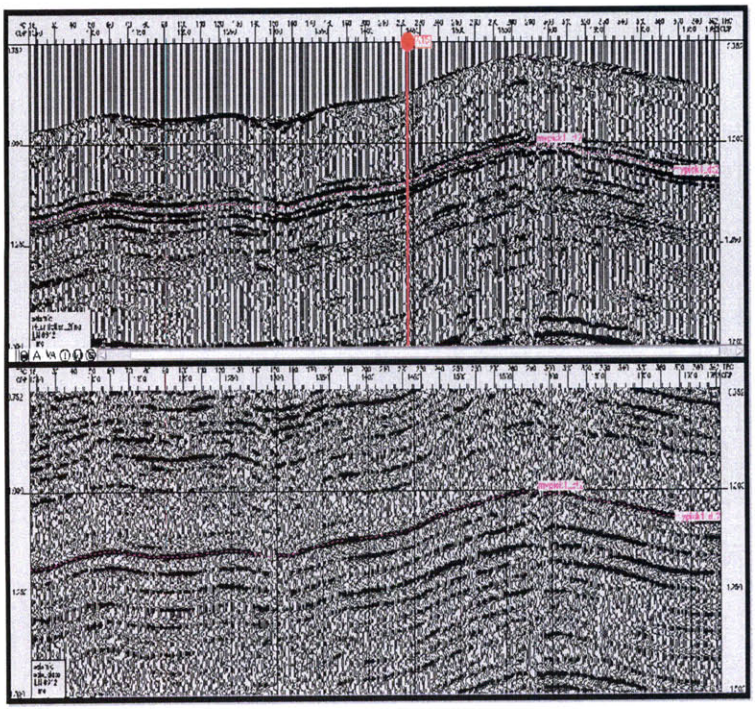

Figure 3-15: Inline through A15: derived reflectivity [Top] , and original seismic section [Bottom].

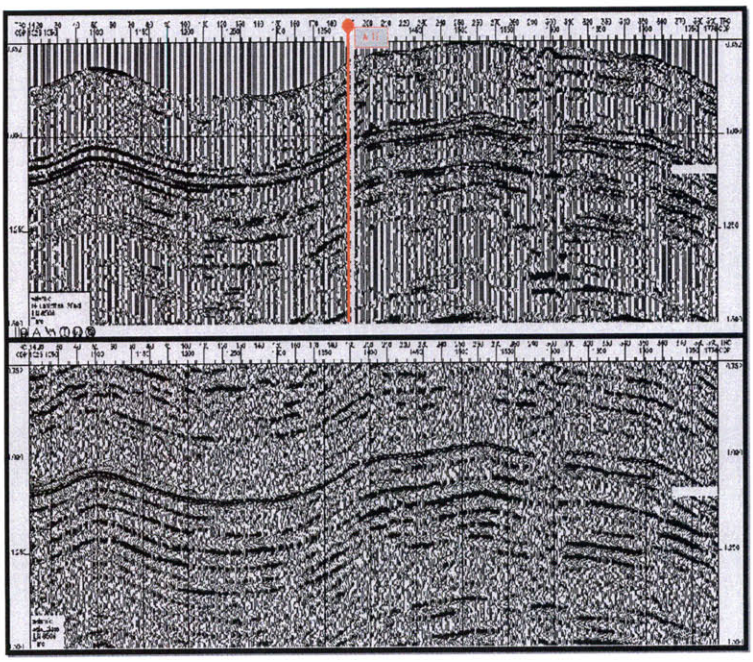

Figure 3-16: Inline through A11: derived reflectivity [Top] , and original seismic section [Bottom].

If the seismic trace is composed of N time samples, where $i = 1 : N$, then

newline

$$R(t_i) = \frac{I_{i+1} - I_i}{I_{i+1} + I_i} \approx \frac{\Delta I}{2I_i}, \tag{3.9}$$

where $\Delta I = I_{i+1} - I_i \Rightarrow I_{i+1} = I_i + \Delta I$.

Assuming that the amplitude is not affected by noise or the shape of the seismic wavelet, the impedance can be derived from Equation 3.9 by integration:

$$\int_0^t R(t_i) = \frac{\Delta I}{2} \int_0^t \frac{1}{I_i} dt$$

$$\frac{2}{\Delta I} \int_0^t R(t_i) dt = \ln I_i + C_1$$

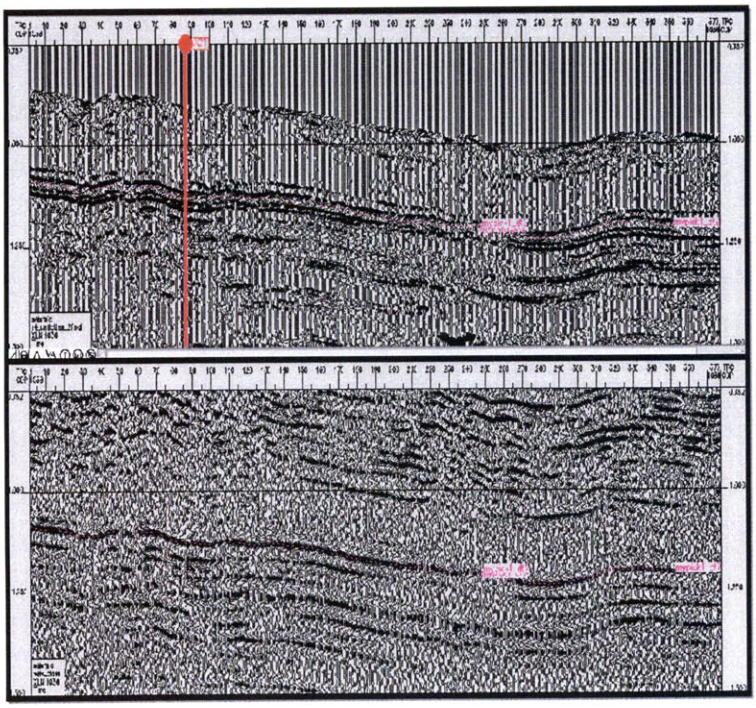

Figure 3-17: Crossline through A21: derived reflectivity [Top] , and original seismic section [Bottom].

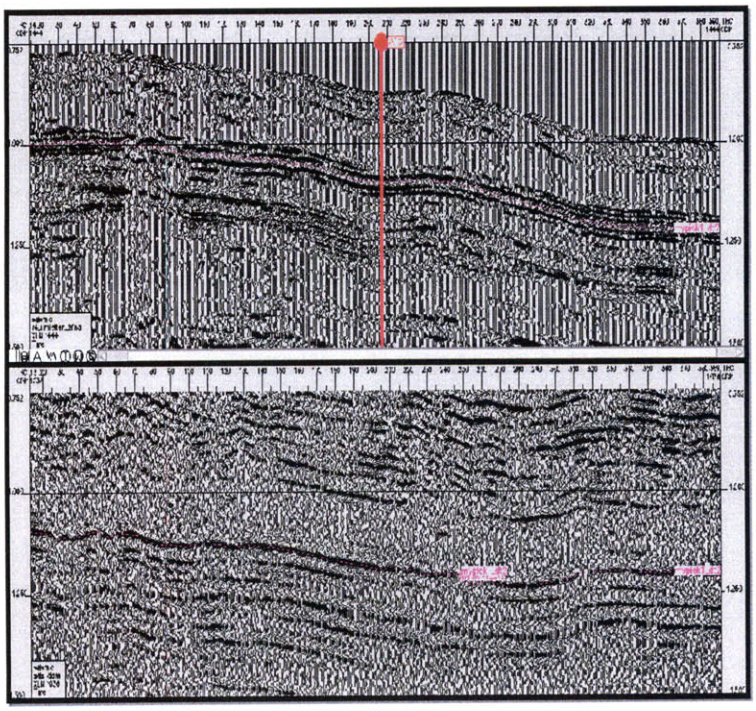

Figure 3-18: Crossline through A15: derived reflectivity result [Top] , and original seismic section [Bottom].

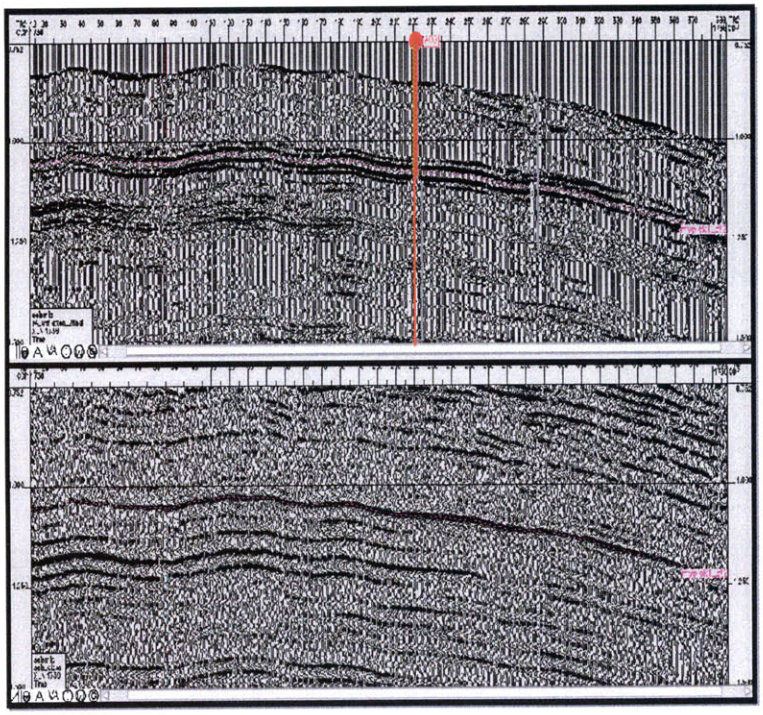

Figure 3-19: Crossline through A09: derived reflectivity [Top] , and original seismic section [Bottom].

$$e^{(\frac{2}{\Delta I}\int_0^t R(t_i)dt)} = I_i e^{(C_1)}$$

$$I_i = e^{(\frac{1}{C_1}e^{(\frac{2}{\Delta I}\int_0^t R(t_i)dt)}}$$

$$I_i = C_2 e^{(C_3\int_0^t R(t_i)dt)}. \tag{3.10}$$

where

$$\begin{aligned} C_2 &= 1/C_1 \\ C_3 &= 2/(DeltaI) \end{aligned} \tag{3.11}$$

$$\ln I_i = \ln C_2 + C_3 \int_0^t R(t_i)dt$$

$$\ln I_i = C_4 + C_3 \int_0^t R(t_i)dt$$

where

$$C_4 = \ln C_2 \tag{3.12}$$

C_3 and C_4 are found by least squares inversion, then $C_1 and C_2 are recalculated.$

The result of the test was promising, as shown in Figure 3-23. The two constants, C_2 and C_3, were derived for every well, then interpolated to generate C_2 and C_3 slices as shown in Figures 3-24 and 3-25. These two slices were part of the inversion process.The result of the inversion was compared to the wells' impedance logs (Figures 3-26, 3-27, and 3-28). The result showed a good match between them.

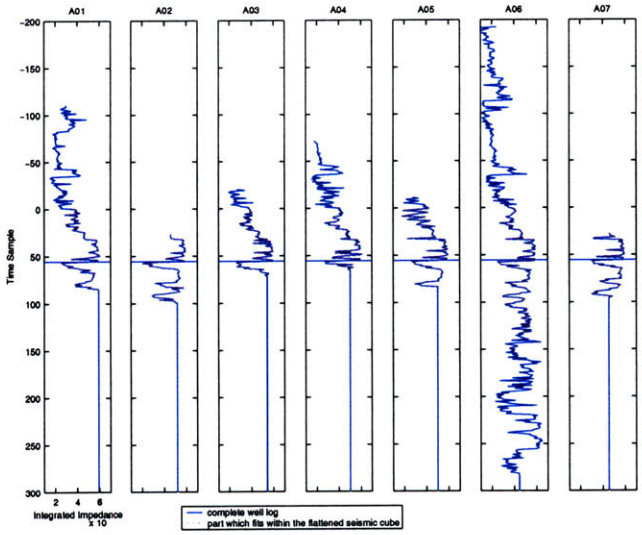

Figure 3-20: Calibrated impedance and seismic trace for wells A01-A07. The blue trace is the complete well impedance log after time conversion and calibration. The red trace is the part that fits within the flattened seismic cube.

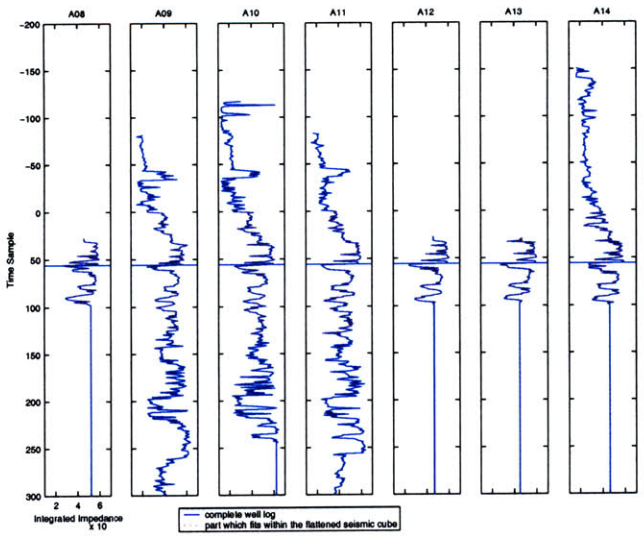

Figure 3-21: Calibrated impedance and seismic trace for wells A08-A14. The blue trace is the complete well impedance log after time conversion and calibration. The red trace is the part that fits within the flattened seismic cube.

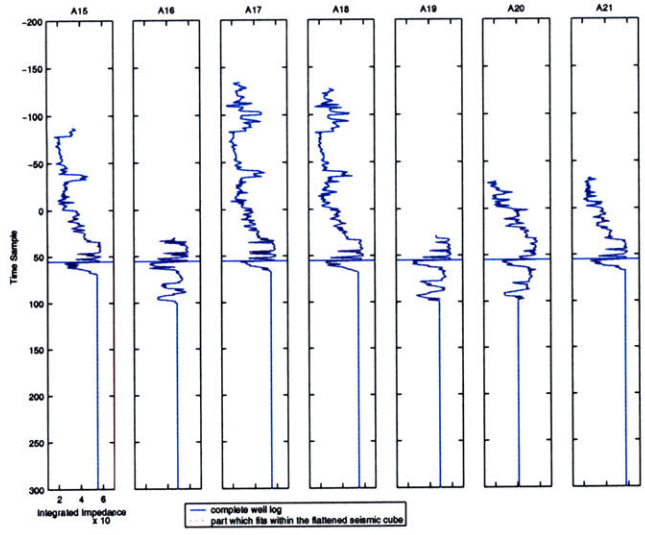

Figure 3-22: Calibrated impedance and seismic trace at wells A15-A21. The blue trace is the complete well impedance log after time conversion and calibration. The red trace is the part that fits within the flattened seismic cube.

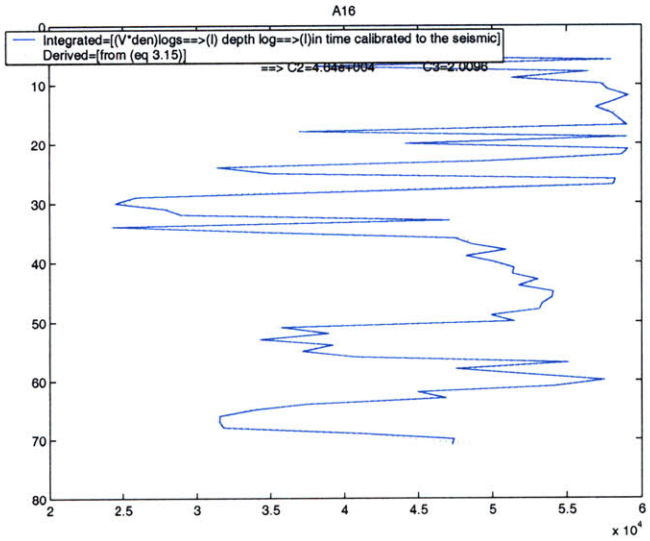

Figure 3-23: Calibrated and derived impedance traces at well A16.

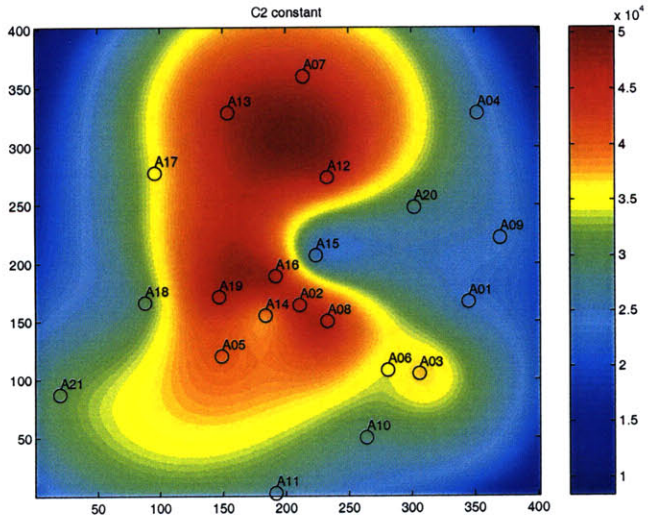

Figure 3-24: C2 slice.

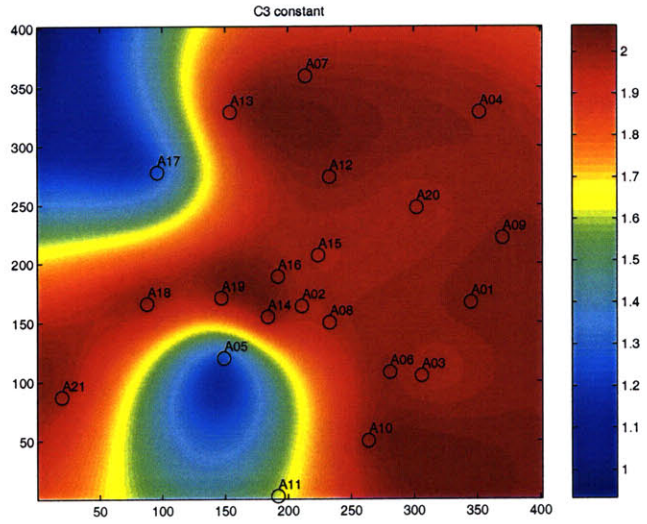

Figure 3-25: C3 slice.

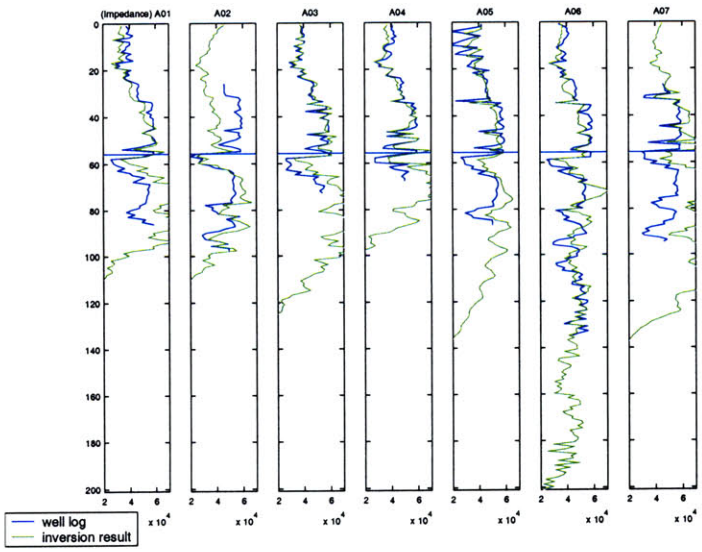

Figure 3-26: A comparison between the well impedance and the calculated impedance for wells A01-A07.

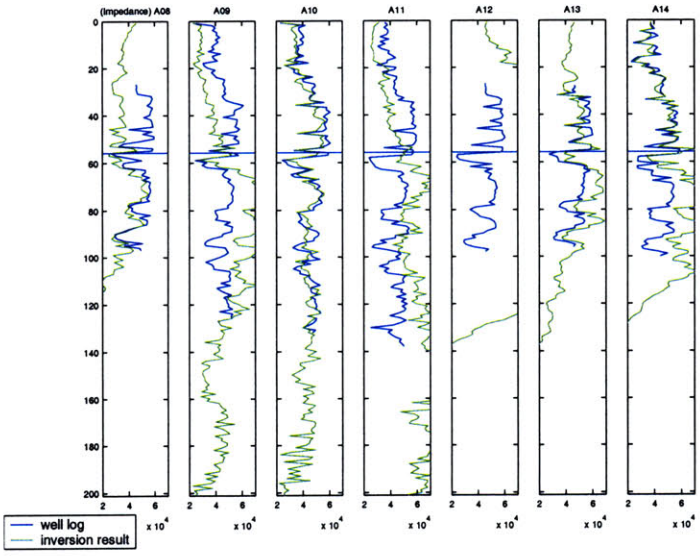

Figure 3-27: A comparison between the well impedance and the calculated impedance for wells A08-A14.

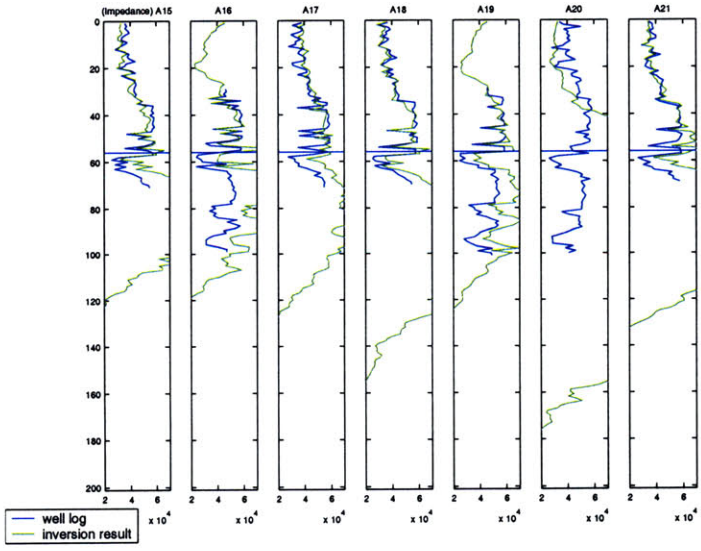

Figure 3-28: A comparison between the well impedance and the calculated impedance for wells A15-A21.

Chapter 4

SEISMIC ATTRIBUTES AND APPLICATIONS

4.1 Seismic Attributes

Seismic attributes analysis in petroleum exploration was first used in the 1970s and 1980s after the development of complex trace theory in the early 1970s. An attribute is defined as a measurement based on seismic data, such as envelope amplitude ("reflection strength"), instantaneous phase, instantaneous frequency, polarity, velocity, dip, dip azimuth, etc (Sheriff, 1994). Seismic attributes are specific measurements of geometric, kinematic, or statistical features derived from seismic data (Chen and Sidney, 1997). Seismic attributes can be defined as all parameters contained in seismics (Coren et al., 2001) .

4.1.1 Classification

Attributes are generally classified based on the information that can be obtained from them 4-1. Time, frequency, amplitude, and attenuation are considered the main sort of information (Brown, 1995). As a broad generalization, time-derived attributes provide structural information, and amplitude-derived attributes provide stratigraphic information (Brown, 1996). Frequency-derived attributes are not yet

well understood but there is widespread optimism that they will provide additional useful reservoir information (Brown, 1996). Attenuation-derived attributes are not widely used so far, but possibly they will be used in the future. A subclassification of attributes can be based on the seismic stack, whether that be a prestack or poststack. The poststack subclassification can be further classified as horizon-extracted or window-extracted. This type of classification was suggested by Alistair Brown in one of his published papers (Brown, 1996).

Chen and Sidney have presented another way of classifying attributes, based on wave kinematics/dynamics and reservoir features. The seismic attribute categories based on wave kinematics/dynamics are amplitude, waveshape, frequency, attenuation, phase, correlation, energy, and ratios. On the other hand, the seismic attribute categories based on reservoir features are bright & dim spot, unconformity & faults, oil- & gas bearing, thin layer reservoir, stratigraphic discontinuity, structural discontinuity, lithologic pinchout, and clastic/limestone differentiation (Figures 4-2 and 4-3).

Another classification of attributes is section-based attributes, event-based attributes, and volume-based attributes. The section-based attributes are ones that use result of special processing such as impedance. The event-based attributes are the attributes that are associated with a surface (picked horizon on the seismic section).

Another classification of attributes is based on the interpretive significance that they represent. They are classified in two main categories: physical attributes and geometrical attributes. The instantaneous attributes belong to the physical attributes category. The attributes which are used in this thesis are instantaneous amplitude, instantaneous phase, instantaneous frequency, and acoustic impedance.

4.1.2 Main Attributes

The instantaneous attributes which are used in this thesis are based on complex trace theory. A complex seismic trace consists of a real part and an imaginary part. To derive the real and imaginary parts, the Hilbert transform of the conventional

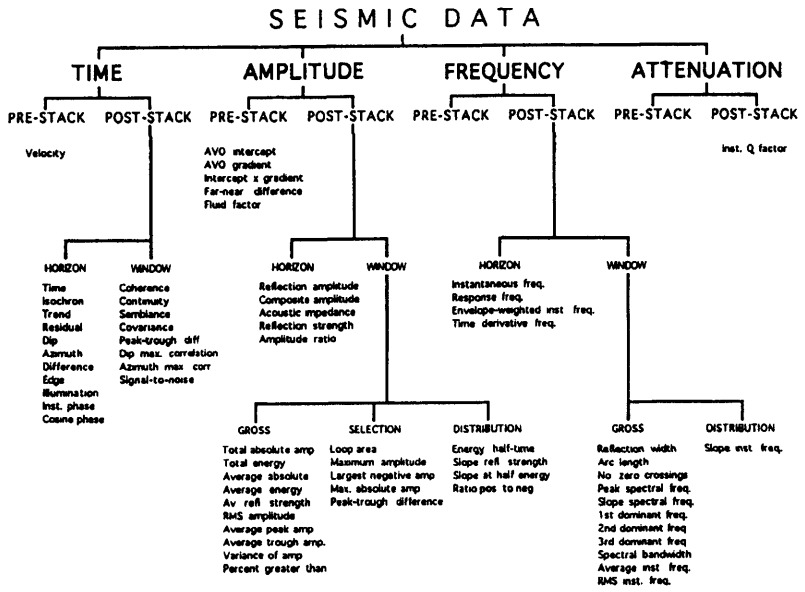

Figure 4-1: Alistair's attributes classification. (Brown, 1996)

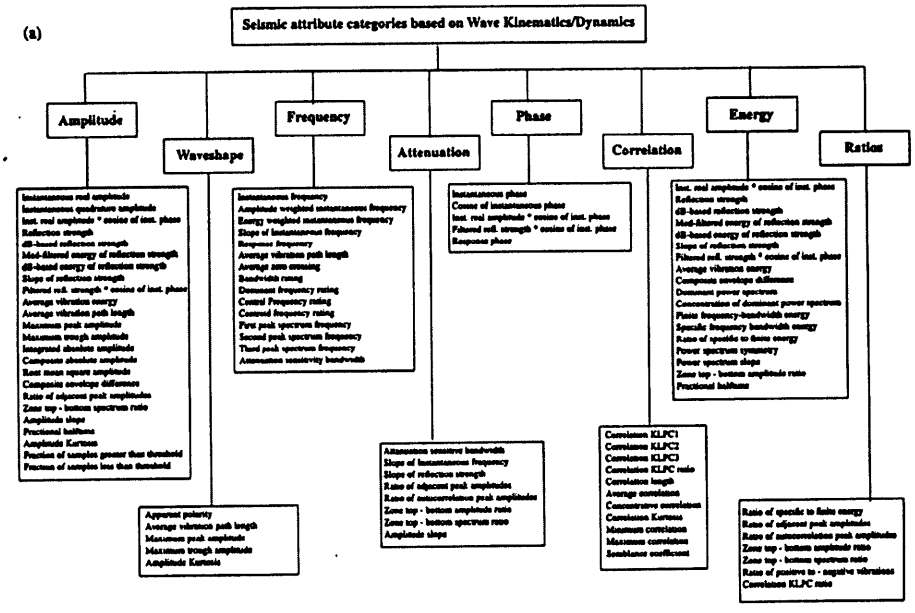

Figure 4-2: (Chen and Sidney, 1997)'s first seismic attribute category.

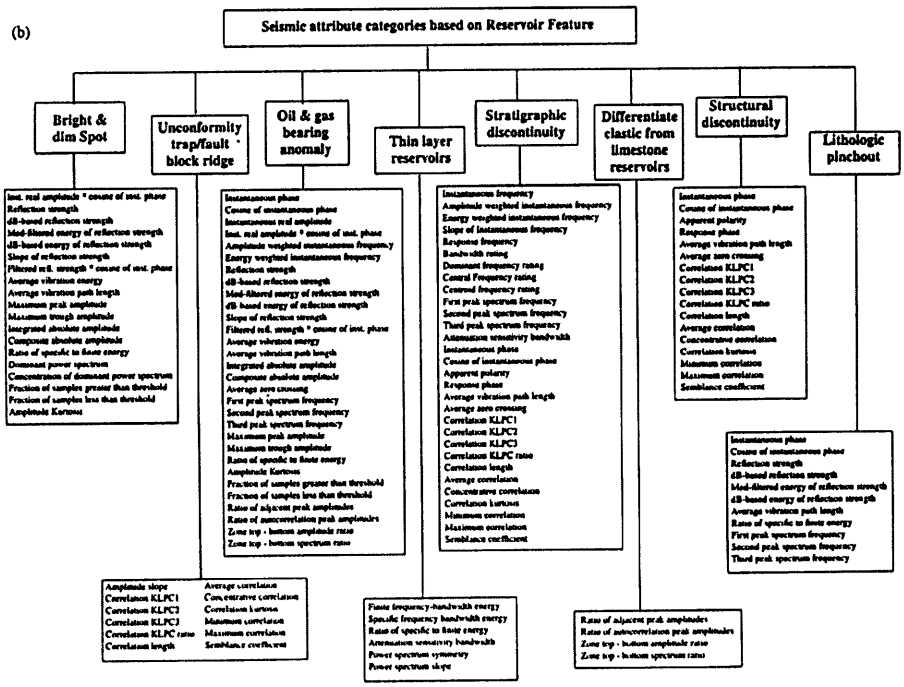

Figure 4-3: (Chen and Sidney, 1997)'s second seismic attribute category.

seismic trace was used. The real and imaginary traces are identical except for being phase shifted by 90° (Figures 4-4 and 4-5). Dealing with a complex seismic trace means dealing with a real trace, an imaginary trace. Since a seismic trace is a causal signal, the imaginary part can be calculated directly from the real part using Hilbert transform.

The complex seismic trace $F(t)$ allows a unique separation of amplitude and phase information (Robertson and Nogami, 1984). The polar form of a complex seismic trace comprises the familiar instantaneous amplitude and phase (Barnes, 1998). The instantaneous amplitude (reflection strength) A(t) represents the envelope of the seismic trace. This is what the complex seismic trace is all about: determining envelopes and associated phases. Instantaneous amplitude and instantaneous phase are called the "fundamental attributes".

Instantaneous amplitude, instantaneous phase, and instantaneous frequency are major attributes that can be computed from complex seismic trace. The term "instantaneous" reveals a concise and quantitative description of a seismic wave at any given

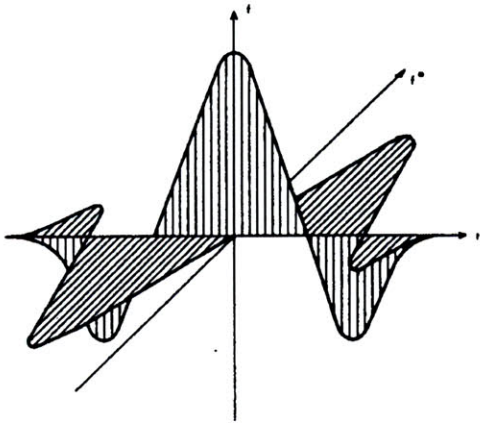

Figure 4-4: The real and imaginary parts of a complex trace. (Taner et al., 1979)

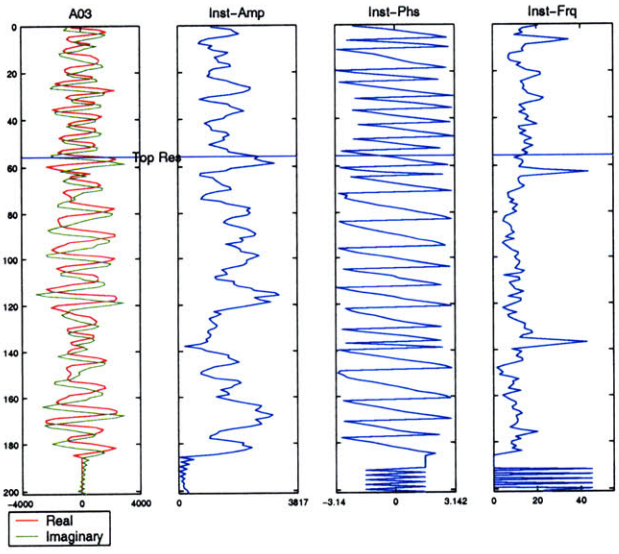

Figure 4-5: 2D view of the complex trace at A03.

time. In other words, these three attributes describe a waveform shape (White, 1991). The instantaneous amplitude gives the magnitude of reflection, the phase describes the polarity, whether it be symmetric, antisymmetric, or somewhere in between, and the frequency defines the times of zero crossings. Attributes of various kinds can be calculated for 3D data to create attribute volumes that can be sliced through just like the original 3D volume itself. The common attributes such as instantaneous amplitude, instantaneous phase, instantaneous frequency, or acoustic impedance generated by one dimensional inversion can be displayed (Sheriff and Geldart, 1994). These major instantaneous attributes, which are the main outcomes of complex signal theory, are widely used in the data interpretational stage; they are displayed as color sections that and can be overlaid over other attributes.

4.2 Estimating Reservoir Porosity Using Attributes

Estimation of reservoir properties can be classified as either deterministic or statistical. A common way for estimating a reservoir property of an area is to interpolate well logs in that area, which is widely known as "kriging." Kriging can produce a reliable result if the area contains closely spaced wells. However, most of the time the area contains only a few control points, so kriging will produces a very smooth map as shown in Figure 4-6. With the availability of 3-D seismic data, the estimation of the reservoir property can be improved by implementing "cokriging" instead of kriging. Cokriging uses the reservoir surface from the 3-D cube as a constraint. It requires a joint model for the matrix of covariance and cross covariance functions (Deutsch and Journel, 1992). Usually, it produces a better constrained result than does kriging (Figure 4-7). Reservoir properties estimation for an area is difficcult from wells alone because these properties are highly stratified and highly variable laterally (?).

This paper presents a third way for estimating reservoir properties, by making use of 3D seismic attributes through linearly weighted sum of attributes.

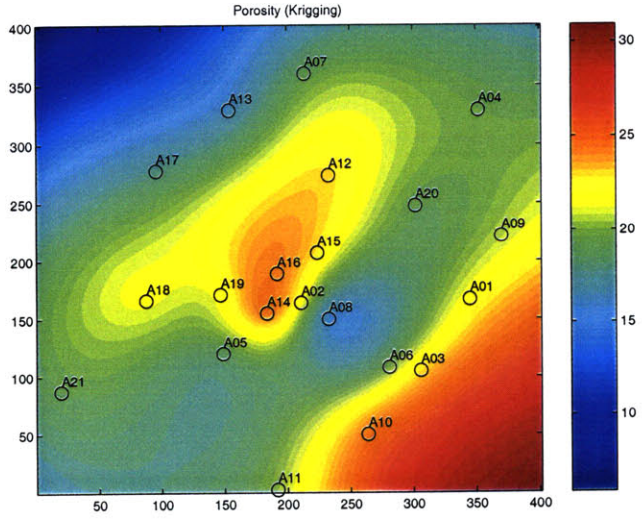

Figure 4-6: Kriging.

The methodology is to use a statistical relationship to estimate the reservoir property. Starting with the available data, well logs and 3D seismic cube, seismic attributes

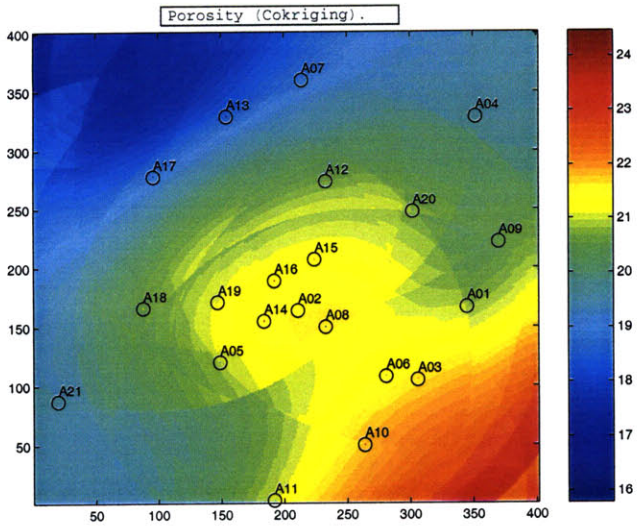

Figure 4-7: Cokriging.

are chosen based on the correlation between the property that is to be estimated and the calculated attributes. Such correlations are shown for a subset of wells in Figures 4-8, 4-9, 4-10, and 4-11. The four small circles in the cross-plot of each attribute represent the top four horizon slices of the reservoir which cover the upper porous zone (approximately 100-150 ft).

The number and types of attributes are selected on the basis of geophysical and petrophysical reasoning. A linearly weighted sum relationship is established:

$$P = w_0 + w_1(ATT_1) + w_2(ATT_2) + w_3(ATT_3) + ... + w_m(ATT_m), \quad (4.1)$$

where

P = the property to be estimated.

ATT_m = the number $(_m)$ of chosen seismic attributes.

w = the weight.

Then, well logs are converted to time and calibrated to the seismic cube. Next, the weights are solved for by using least squares algorithm (Equation 4.2).

$$(P = Sw) \;\Rightarrow\; (S^T P = S^T S w) \;\Rightarrow\; (w = (S^T S)^{-1} S^T P). \tag{4.2}$$

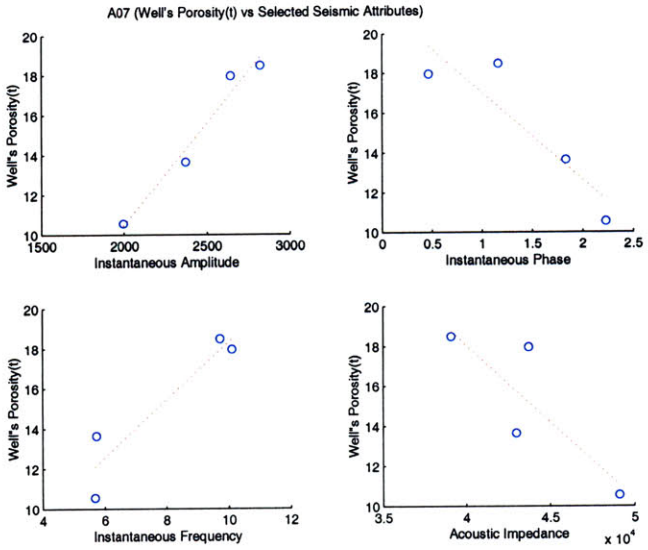

Figure 4-8: Cross-plots between the selected seismic attributes and the well's porosity for well A07.

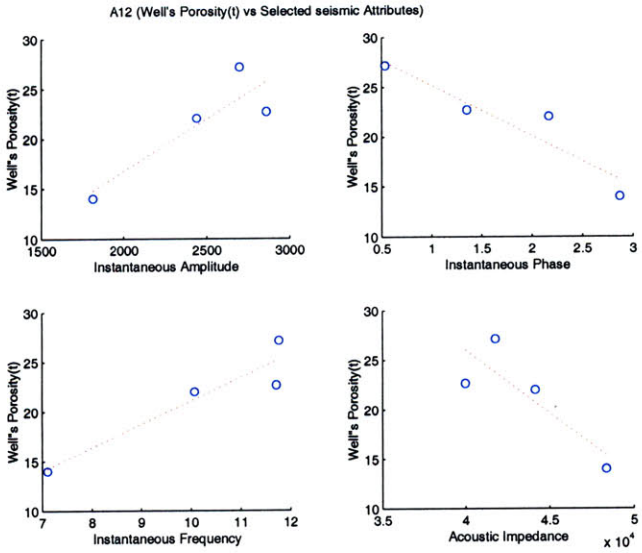

Figure 4-9: Cross-plots between the selected seismic attributes and the well's porosity for well A12.

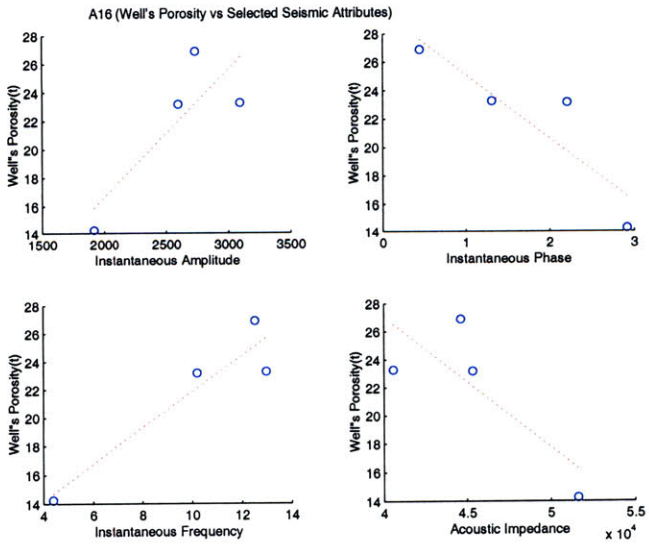

Figure 4-10: Cross-plots between the selected seismic attributes and the well's porosity for well A16.

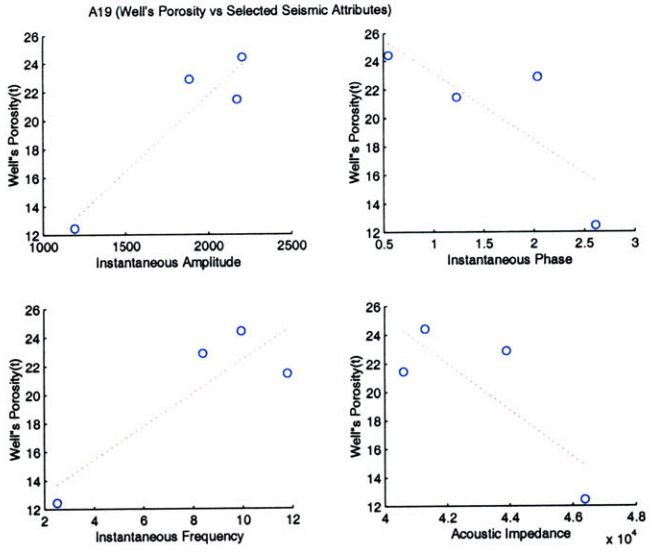

Figure 4-11: Cross-plots between the selected seismic attributes and the well's porosity for well A19.

4.2.1 Porosity Estimation

The main objective is to predict the porosity of the reservoir by the described method. The porosity of a rock sample can be determined from a measurement of its bulk density (Bradley, 1987). The fundamental equation that relates the rock density to the porosity is:

$$\rho_{rock} = \rho_{grain}(1 - \phi) + \rho_{fluid}\phi, \tag{4.3}$$

where

ρ = density.

ϕ = porosity.

The basemap of the studied area is shown in Figure 4-12. The method was implemented using the 3D seismic and well data to estimate a regional distribution of the reservoir's upper zone porosity. From well data, the NPHI log was not available for every well and showed inconsistent values at some well locationsdue to lack of

calibration. Therefore, the porosity logs were derived for the 21-wells using Wyllies equation:

$$\Phi(z) = \frac{\Delta t - \Delta t_m}{\Delta t_f - \Delta t_m}, \tag{4.4}$$

where

$\Phi(z)$ = the porosity log as a function of depth.

Δt = the sonic transit time from log.

Δt_m = the matrix transit time value.

Δt_f = the fluid transit time value.

Figure 4-13 shows the calculated porosity log compared to the NPHI log for one well. It also shows the reservoir zone between two bars. These porosity logs were then converted from depth to time and calibrated with the 3D seismic volume. The volume was flattened previously at the reservoir level to make calibration of the wells' data easier. Four attributes were used: instantaneous amplitude, instantaneous phase, instantaneous frequency, and acoustic impedance. The basic instantaneous attributes were derived using the complex trace theory. The acoustic impedance volume was derived by inverting the reflectivity volume by integration using least squares (Chapter 3). Using Equation (4.2), the five weights (w_0 *to* w_4) were calculated by least squares (Equation 4.2). A comparison between the wells porosity and the model porosity for the 21 wells is shown in Figures 4-14 to 4-16. Figure 4-17 shows a crossplot between the wells porosity and model porosity for 12 time samples below the top of the reservoir, then it zooms into the reservoir time-samples. The next step was to use weights (w_0 *to* w_4) in Equation 4.2 to predict the final average porosity map for the upper reservoir zone of the field (next chapter).

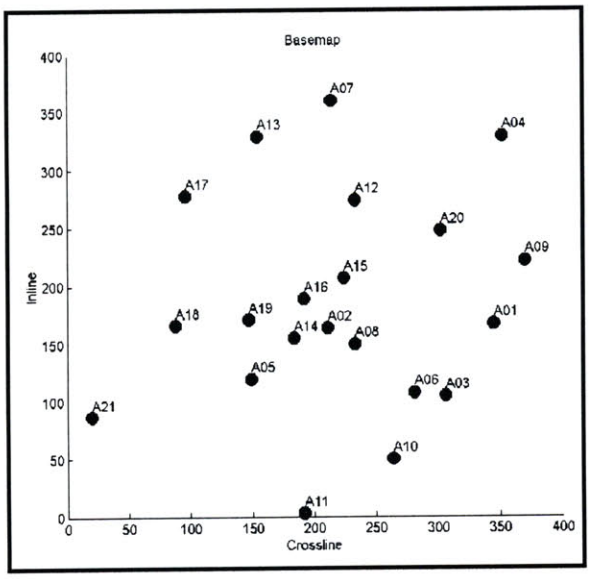

Figure 4-12: Basemap.

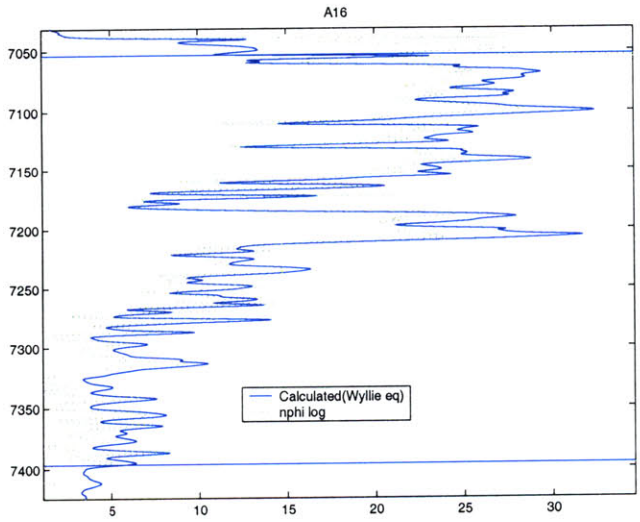

Figure 4-13: Calculated porosity log and NPHI log for one of the wells.

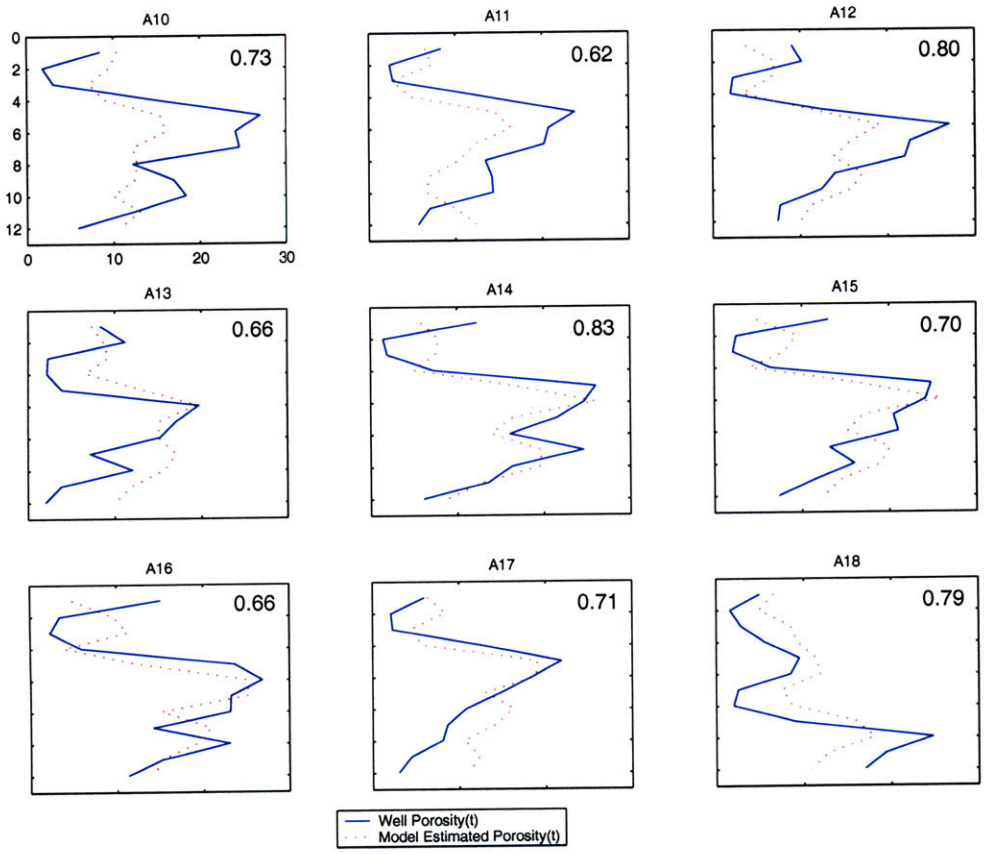

Figure 4-14: A comparison between the well porosity and the model porosity for wells A01-A09. The correlation coefficient between the two porosity logs (well and model) is shown in the upper right corner for every well.

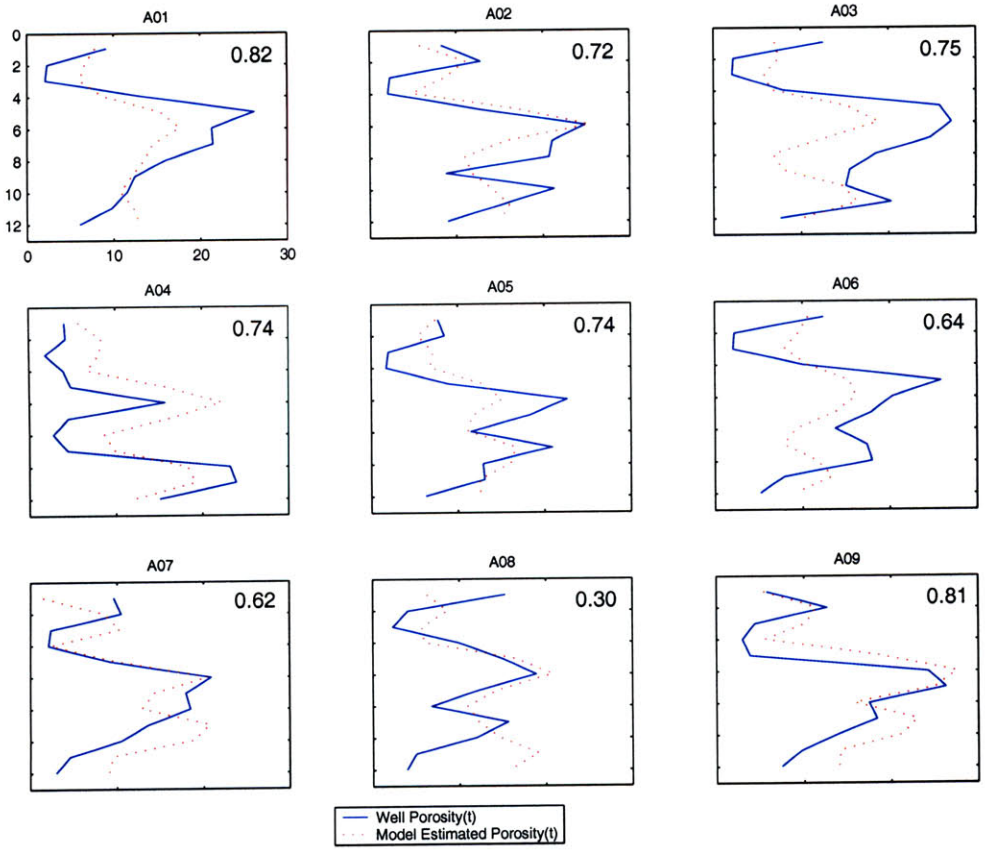

Figure 4-15: A comparison between the well porosity and the model porosity for wells A10-A18. The correlation coefficient between the two porosity logs (well and model) is shown in the upper right corner for every well.

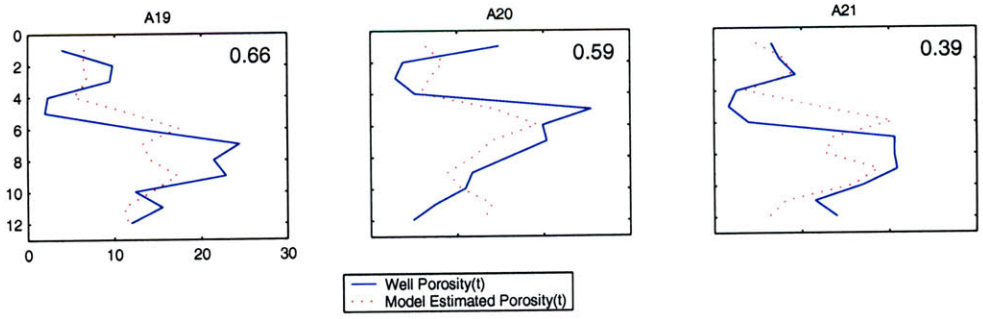

Figure 4-16: A comparison between the well porosity and the model porosity for wells A19-A21. The correlation coefficient between the two porosity logs (well and model) is shown in the upper right corner for every well.

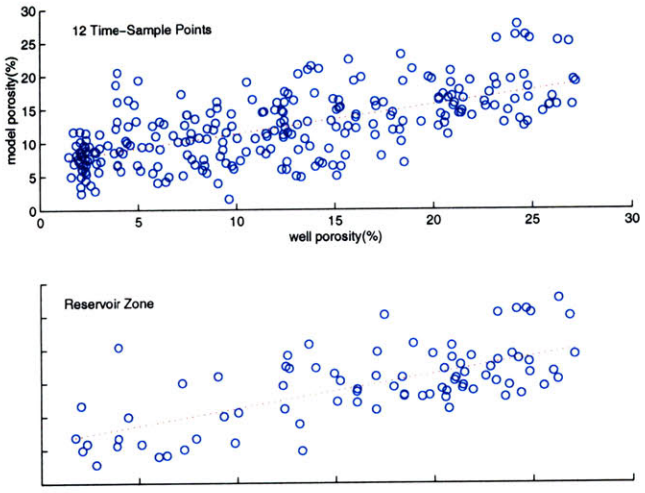

Figure 4-17: A crossplot between the well porosity and the model porosity for 12 time sample points at every well [top]; time-samples within the reservoir [middle]; time-sample points near the maximum porosity peak [bottom].

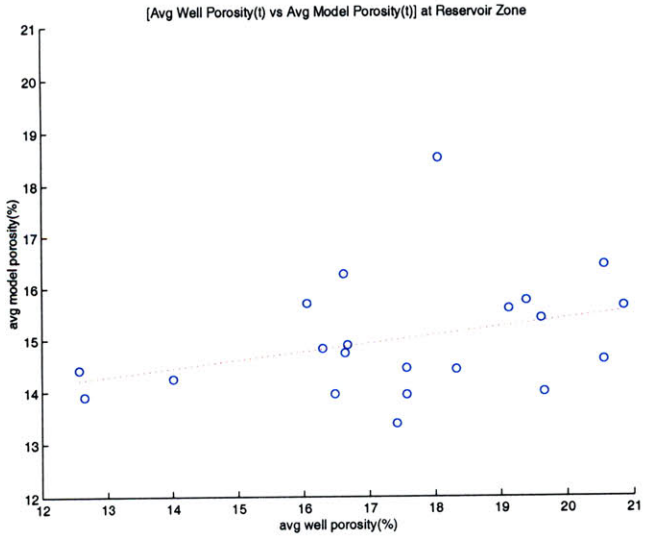

Figure 4-18: A crossplot between the average well porosity and the average model porosity for the 21 wells.

Chapter 5

APPLICATIONS TO RESERVOIR: PROPERTIES DISTRIBUTION

Given the attributes discussed in chapter 4, reservoir properties can be calculated from seismic data. Two methods will be used. First, will be estimation of porosity from weighted attributes and the second will be use of similarity.

5.1 Porosity Distribution

The weights $(w_0, w_1, w_2, w_3, and w_4)$ in Equation 4.2 were calculated based on the 21 well-locations then used to predict the areal distribution of the reservoir porosity. Figure 5-1 shows the porosity distribution map implemented by the linear regression method which showed more reliable and accurate than were the results from kriging or cokriging methods.

Seismic reflection patterns are a function of acoustic impedance contrasts. In many case studies, only one parameter, either velocity or density, is known and the other has yo be estimated using empirical functions or formulas (Palaz and Marfurt, 1997). Using Equation 4.5, the reservoir density map was estimated from the porosity map at the reservoir level (Figure 5-2). Since porosity and density are related (Equation

4.4), a reservoir density map can be generated. Density is important for calculating acoustic impedance. Figures 5-1 and 5-2 the correlation of low density with high porosity

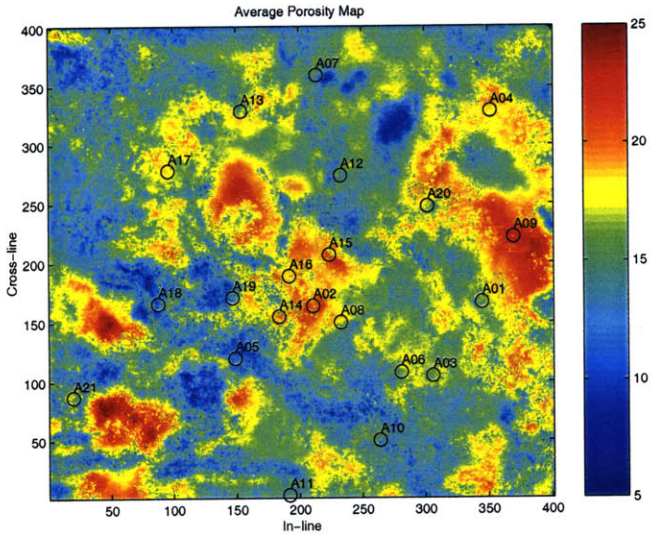

Figure 5-1: Reservoir average porosity map.

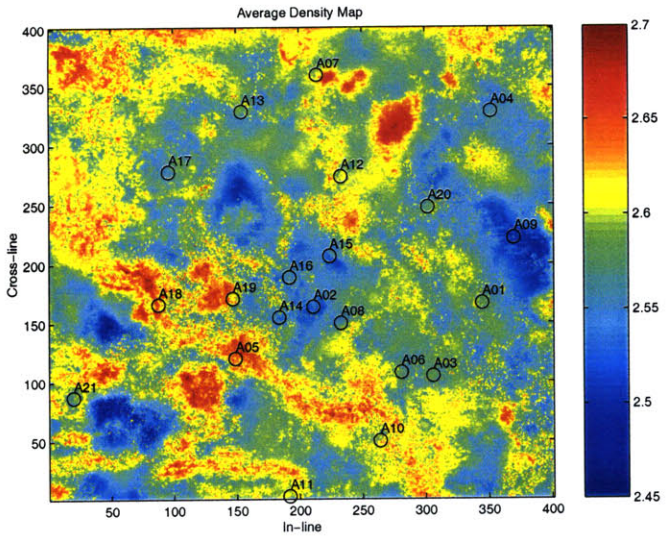

Figure 5-2: Reservoir average density map.

5.2 Similarity Map

Each attribute may reveal different subtle information that cannot be recognized in the conventional seismic section. When dealing with multiple attributes an approach is needed to handle and combine information from different attributes. An example was shown in section 5.1. Similarity map is another way of handling multi-attributes to exhibit similar reservoir areas referenced to a selected location (high producing, dry, or wet well). It also helps with the reservoir characterization by showing the general trends and patterns of the reservoir.

The well data and the 3D seismic data were tied together on the top-reservoir level. The top of the reservoir was picked seismically over the area then flattened. Four different attributes volumes were generated then used in the study: instantaneous amplitude, instantaneous phase, instantaneous frequency, and acoustic impedance. The main steps of the method are shown in Figure 5-3.

A horizon-slice at the reservoir was extracted from each of the attribute volumes. First, well A14 (high producing well) was chosen as a reference well (Figure 5-4). The selection of the reference well could be the highest production well, the lowest

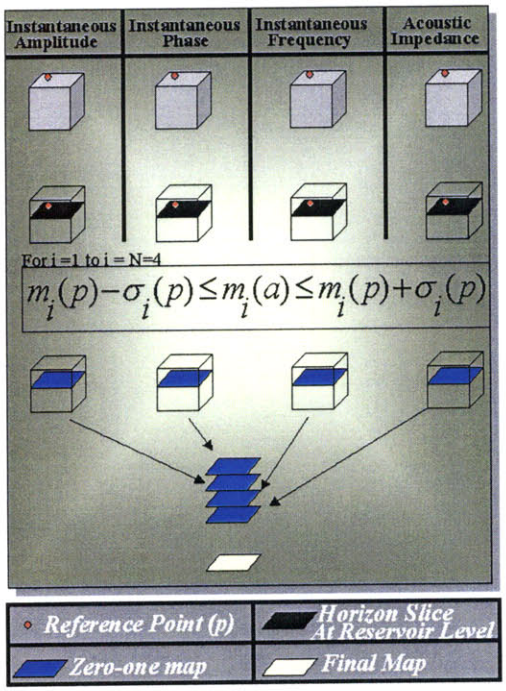

Figure 5-3: The main steps of the similarity method.

production well, a dry well, or any other classification depending on the objective of the analysis. The objective was to map the reservoir of the field based on the reference point A14 for possible high production areas. A radius value around the well was chosen then used to calculate the mean and standard deviation of the reference point(p=A14) within the radius(r) from the extracted horizon slice for each of the attributes. The output of the first step was (N) different reference means and reference standard deviations for the same reference point(p); (N=4) is the number of attributes that were used in the study. The next step was to calculate a zero-one matrix from the extracted horizon-slice for each attribute based on a statistical criterion that would assign either zero or one to every node for a given horizon-slice. Each horizon-slice had (160801=401x401) nodes. The criteria was as follow:

If [mean (reference point)-standard deviation (reference point)] < mean (node) < [mean (reference point)+standard deviation (reference point)],

then the node was assigned one. Otherwise, zero was assigned to the node. Finally,

zero-one maps were summed into one single map. The zero-one maps are shown in Figures 5-5 to 5-8. The red areas in the zero-one maps indicate that the criterion was satisfied and the value 'one' was assigned to each node in that red areas. The four attributes reveal different information and their zero-one maps show different distributions that help interpreters to correlate/relate each map to other types of information such as production or geologic information. The final map was obtained by summing the zero-one maps (Figure 5-9). The red color in the final similarity map exhibited areas of highest similarity to the chosen reference location A14 which refers to possible high producing areas. The similarity map also showed the general trend of structures in the field to the NW-SE direction. The result indicates that the method is an effective tool in the reservoir characterization and studies. Comparing the similarity map (Figure 5-9) with the porosity map (Figure 5-1) showed a general correlation between the high porosity areas with the red zones (high-production) in the similarity.

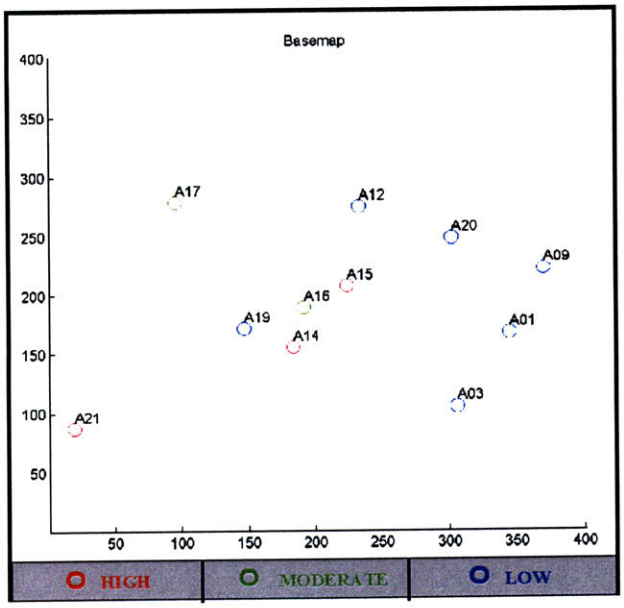

Figure 5-4: Wells classification based on production rate.

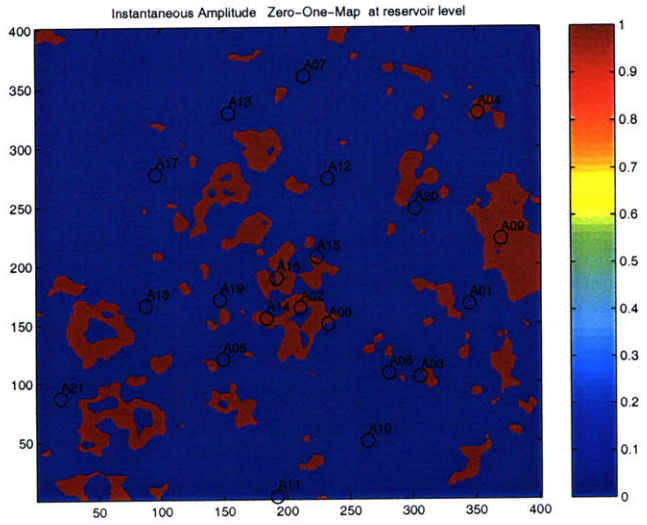

Figure 5-5: Zero-one map of instantaneous amplitude.

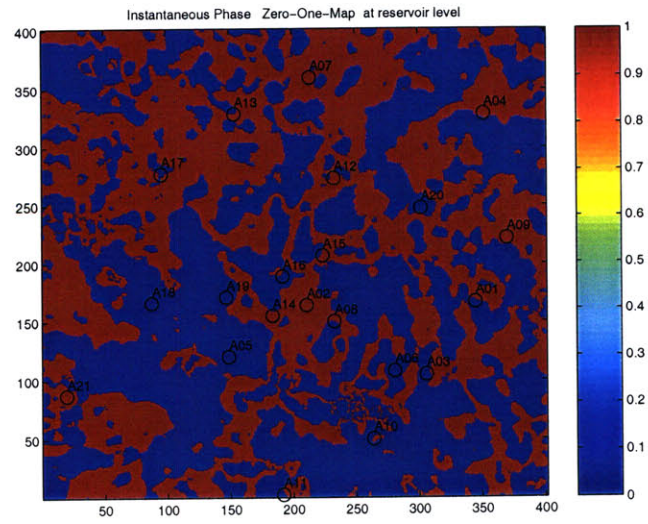

Figure 5-6: Zero-one map of instantaneous phase.

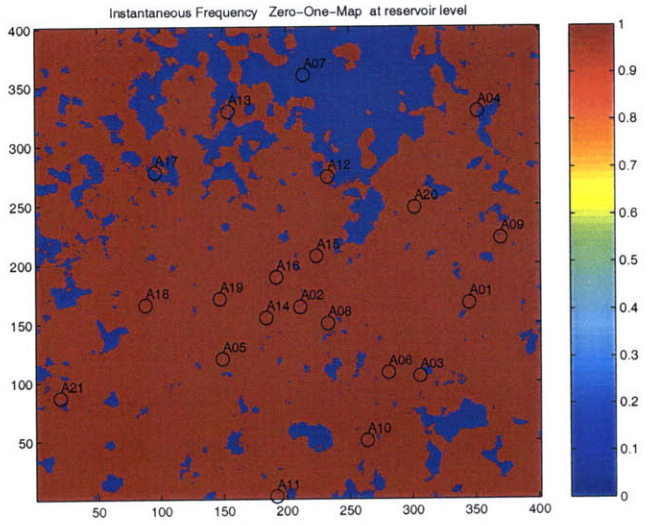

Figure 5-7: Zero-one map of instantaneous frequency.

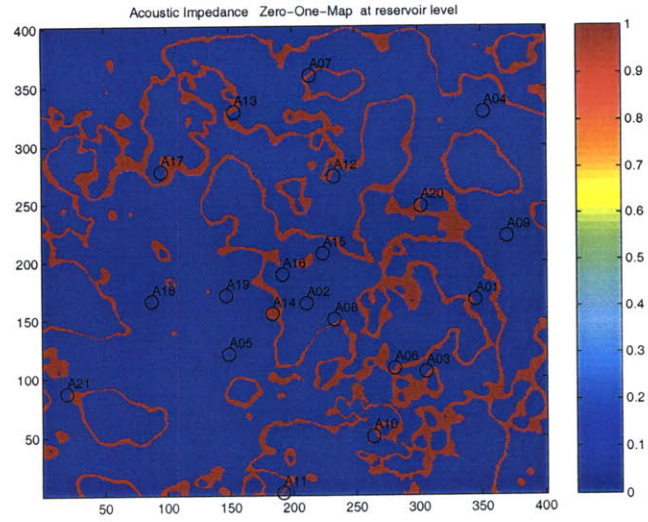

Figure 5-8: Zero-one map of impedance.

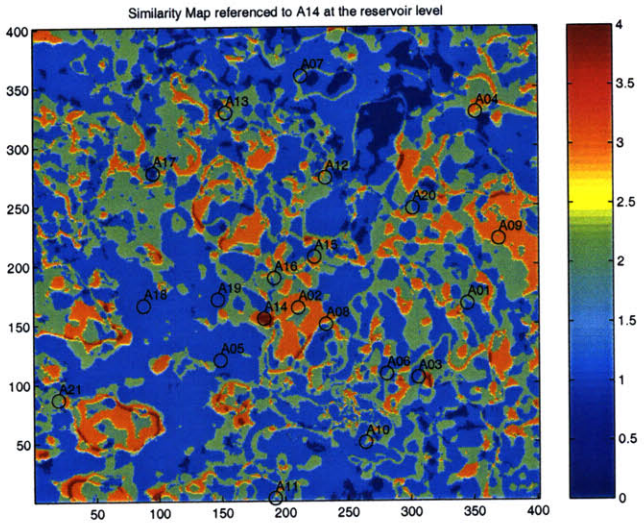

Figure 5-9: The Similarity Map.

Chapter 6

CONCLUSIONS

Three dimensional seismic data and well data from the eastern region of Saudi Arabia were used to acquire reflectivity and acoustic impedance data by inversion. The seismic and well data were also used to implement 3D attribute analysis.

The joint kriging-deconvolution method to derive reflectivity from the seismic data improved the overall resolution of the data and increased the signal-to-noise ratio. A comparison between the amplitude spectrum of the seismic trace to the amplitude spectrum of the reflectivity showed an improvment after the joint inversion.

The acoustic impedance which was acquired from reflectivity by an inverse problem using least squares showed a good match between the well impedance and the calculated impedance. It is a direct and fast method because it uses the reflectivity data as a direct input, then integrates it with respect to time.

Single and multi-attributes analyses have been used with success in reservoir characterization. Two applications of multi-attributes analysis were implemented with the data used in this study: a linear regression model and a similarity map. The final similarity map showed the right trends of the structures in the area and refered to areas of better reservoir quality. The two applications are powerful tools for characterizing reservoirs.

Appendix A:JOINT KRIGING-DECONVOLUTION INVERSION

This inversion was implemented to the data. The results are shown in chapter 3. The method was developed by Kane and more information can be found in his paper . The following is the derivation to the final equation in two different approachs.

$$
\begin{array}{rcl}
s = Hr + n_H, & d = Pr + n_P, & Lr = n_L \\
s = Hr + \sigma_H n_H' , & d = Pr + \sigma_P n_P' , & Lr = \sigma_L n_L' \\
n_H' = \frac{1}{\sigma_H}(s - Hr) , & n_P' = \frac{1}{\sigma_P}(d - Pr) , & n_L' = \frac{1}{\sigma_L} Lr \\
\|n_H'\| = \frac{1}{\sigma_H}(s - Hr)^T \frac{1}{\sigma_H}(s - Hr) , & \|n_P'\| = \frac{1}{\sigma_P}(d - Pr)^T \frac{1}{\sigma_P}(d - Pr) , & \|n_L'\| = \frac{1}{\sigma_L}(Lr)^T \frac{1}{\sigma_L}(Lr) \\
\|n_H'\| = \frac{1}{{\sigma_H}^2}(s - Hr)^T (s - Hr) , & \|n_P'\| = \frac{1}{{\sigma_P}^2}(d - Pr)^T (d - Pr) , & \|n_L'\| = \frac{1}{{\sigma_L}^2}(Lr)^T (Lr) \\
= \frac{1}{{\sigma_H}^2}(s^T s - s^T Hr - r^T H^T s + r^T H^T Hr) , & \frac{1}{{\sigma_P}^2}(d^T d - d^T Pr - r^T P^T d + r^T P^T Pr) , & \frac{1}{{\sigma_L}^2}(r^T L^T Lr) \\
= \frac{1}{{\sigma_H}^2}(s^T s - (Hr)^T s - r^T H^T s + r^T H^T Hr) , & \frac{1}{{\sigma_P}^2}(d^T d - (Pr)^T d - r^T P^T d + r^T P^T Pr) , & \frac{1}{{\sigma_L}^2}(r^T L^T Lr) \\
= \frac{1}{{\sigma_H}^2}(s^T s - r^T H^T s - r^T H^T s + r^T H^T Hr) , & \frac{1}{{\sigma_P}^2}(d^T d - r^T P^T d - r^T P^T d + r^T P^T Pr) , & \frac{1}{{\sigma_L}^2}(r^T L^T Lr) \\
= \frac{1}{{\sigma_H}^2}(s^T s - 2r^T H^T s + r^T H^T Hr) , & \frac{1}{{\sigma_P}^2}(d^T d - 2r^T P^T d + r^T P^T Pr) , & \frac{1}{{\sigma_L}^2}(r^T L^T Lr)
\end{array}
$$

Combining the three equations:

$$= \frac{1}{{\sigma_H}^2}(s^T s - 2r^T H^T s + r^T H^T Hr) + \frac{1}{{\sigma_P}^2}(d^T d - 2r^T P^T d + r^T P^T Pr) + \frac{1}{{\sigma_L}^2}(r^T L^T Lr)$$

the solution is found by taking the derivative with respect to 'r' then equalizing it to zero

$$= \frac{-2}{{\sigma_H}^2} H^T s + \frac{2}{{\sigma_H}^2} H^T H r - \frac{2}{{\sigma_P}^2} P^T d + \frac{2}{{\sigma_P}^2} P^T P r + \frac{2}{{\sigma_L}^2} L^T L r = 0$$

$$(\frac{1}{{\sigma_H}^2} H^T H + \frac{1}{{\sigma_P}^2} P^T P + \frac{1}{{\sigma_L}^2}) r = \frac{1}{{\sigma_H}^2} H^T s + \frac{1}{{\sigma_P}^2} P^T d$$

Minimizing the number of σ's by multiplying both sides by ${\sigma_P}^2$:

$$(\lambda_1 H^T H + P^T P + \lambda_2 L^T L) r = \lambda_1 H^T s + P^T d. \qquad \text{(A.1)}$$

where $\lambda_1 = \frac{{\sigma_P}^2}{{\sigma_H}^2}$ and $\lambda_2 = \frac{{\sigma_P}^2}{{\sigma_L}^2}$. λ_1 and λ_2 express the relative importance of fitting the seismic data to honor the well data, and the relative smoothness to honor the well data, respectively. In other words, high λ_1 means deconvolution is weighted more than kriging. In addition, if the limit of $\lambda_2 \mapsto 0$, then the result is a true deconvolution process. Due to the sensitivity of λ_1 and λ_2 , these parameters should be chosen carefully in the case of joint operations (deconvolution and kriging) to assure a balance between the two operations. The three σ's were grouped into two λ's to minimize the amount of computation in the conjugate gradient algorithm (Kane, 2000).

Another approach to the solution is to think in terms of Gaussian distribution:

First, each of the three sigmas $({\sigma_H}^2, {\sigma_P}^2, and\ {\sigma_L}^2)$ is assigned a probability distribution since each one of the sigmas is a random vector. The multi-dimensional Gaussian distribution was used:

$$f_H(n_H|r,s) = \frac{1}{2\pi det(C_H)^{N/2}} e^{-1/2(s-Hr)^T {C_H}^{-1}(s-Hr)} \qquad \text{(A.2)}$$

$$f_P(n_P|r,d) = \frac{1}{2\pi det(C_P)^{N/2}} e^{-1/2(s-Pr)^T {C_P}^{-1}(s-Pr)} \qquad \text{(A.3)}$$

and

$$f_L(n_L|r) = \frac{1}{2\pi det((\frac{1}{{\sigma_L}^2} L^T L)^{-1})^{N/2}} e^{\frac{-1}{2{\sigma_L}^2}(r^T L^T L r)} \Rightarrow f_prior(r) = \frac{1}{(2\pi det(C_L))^{N/2}} e^{\frac{-1}{2} r^T {C_L}^{-1}} \qquad \text{(A.4)}$$

The notation s(X | Y) represents the probability of vector X conditioned on the observed vector Y. $C_H = (\sigma_H{}^2 I)$ *and* $C_P = \sigma_P{}^2 I$, where I is the identity matrix. Other distributions can be used if there is prior knowledge on the distribution of noise. Equation A.4 is the prior equation, which is widely used in Bayesian inversion, where it describes the state of prior knowledge on the quantity to be estimated before the experiment takes place.

Next, step is to maximize the probability in Equations A.2, A.3, and A.4 by posterior distribution in order to find the best (r) possible. This is done in two steps: (1)multiplying and then (2)normalizing the three functions:

$$f_post(r|s,d) = f_H(n_H|r,s)\ f_P(n_P|r,d)\ f_prior(r) \Rightarrow = ke^{-\epsilon(r|s,d)}, \qquad \text{(A.5)}$$

where (k) is a normalizing constant and (ϵ) is:

$$\epsilon(r|s,d) = 1/2(\frac{1}{\sigma_H{}^2}(s-Hr)^T(s-Hr)+\frac{1}{\sigma_P{}^2}(d-Pr)^T(d-Pr)+\frac{1}{\sigma_L{}^2}r^T L^T Lr). \quad \text{(A.6)}$$

Maximizing Equation (A.5) $\Leftrightarrow$ minimizing Equation (A.6).

The solution is found by equalizing the derivative (with respect to r) of Equation (A.6) to zero:

$$\frac{\partial\epsilon(r|s,d)}{\partial r} = (\frac{1}{\sigma_H{}^2}H^T H + \frac{1}{\sigma_P{}^2}P^T P + \frac{1}{\sigma_L{}^2}L^T L)r - \frac{1}{\sigma_H{}^2}H^T s - \frac{1}{\sigma^2}PTd = 0$$

Rearranging,

$$(\frac{1}{\sigma_H{}^2}H^T H + \frac{1}{\sigma_P{}^2}P^T P + \frac{1}{\sigma_L{}^2}L^T L)r = \frac{1}{\sigma_H{}^2}H^T s + \frac{1}{\sigma_P{}^2}P^T d.$$

Multiplying by $\sigma_P{}^2$,

$$(\lambda_1 H^T H + P^T Pr + \lambda_2 L^T L)r = \lambda_1 H^T s + P^T d, \Longleftrightarrow Ar = b. \qquad \text{(A.7)}$$

Appendix B:HILBERT TRANSFORM

Hilbert transform was used in attribute analysis. This appendix provides a concise summary of equations.

The real seismic trace = $f(t) = A(t)\cos\theta(t)$.

The imaginary seismic trace = $f'(t) = A(t)\sin\theta(t)$.

The complex trace = $F(t) = A(t)\cos\theta(t) + iA(t)\sin\theta(t)$.

A(t) and $\theta(t)$ are the instantaneous amplitude and instantaneous phase respectively.

The A(t) is also called 'reflection strength'.

$A(t) = [f^2(t) + f'^2(t)]^{1/2} = A(t)e^{i\theta(t)}$.

$\theta(t) = tan^{-1}[f'(t)/f(t)]$.

The instantaneous frequency = $w(t) = d\theta(t)/dt = d/dt[\tan^{-1}(f'(t)/f(t))]$.

If it is assumed that the real trace is defined for $-\infty$ < f(t) < ∞, then it can be represented by the Fourier formula:

$$f(t) = \int_{-\infty}^{\infty} B(w)e^{+itw}dw = \int_0^w C(w)\cos[wt + \phi(w)]dw,$$

where $C(w) = 2|B(w)|$ and $\phi(w) = argB(w), w > 0$. Then,

$$f'(t) = \int_0^w C(w) \sin[wt + \phi(w)] dw,$$

$$\text{and} \quad F(w) = \int_0^w e^{i[wt+\phi(w)]} dw. \tag{B.1}$$

The complex trace can be found by: Fourier transforming the real trace, then zeroing the amplitude for negative frequencies and doubling the amplitude for positive frequencies, and then inverse Fourier transforming.

The imaginary part of a complex trace can be generated from the Hilbert transform.

Bibliography

Aki, K. and P. Richards, *Quantitative Seismology*, W.H. Greeman and Co., 1980.

Barnes, A. E., The complex seismic trace made simple, *The Leading Edge, 17*, 473-476, 1998.

Bradley, H., *Petroleum Engineering Handbook*, SPE, 1987.

Brown, A., Teaching yes, practice no, *The Leading Edge, 14*, 1039-1041, 1995.

Brown, A., Seismic attributes and their classification, *The Leading Edge, 15*, 1090, 1996.

Cantrell, D. and R. Hagerty, Microporosity in Arab formation carbonates, Saudi Arabia, *GeoArabia, 4*, 129-154, 1999.

Castagna, J., Communication, integration and the next geophysical frontier, *The Leading Edge, 13*, 32-36, 1994.

Chen and S. Sidney, Seismic attribute technology for reservoir forecasting and monitoring, *The Leading Edge*, 445-456, 1997.

Coren, F., V. Volpi, and U. Tinivella, Gas hydrate physical properties imaging by multi-attribute analysis-black ridge bsr case history, *Marine Geology J., 178*, 197-210, 2001.

Deutsch, C.V. and A.G. Journel, *GSLIB Geostatistical Software Library and Users Guide*, Oxford University Press, 1992.

Kane, J., Simultaneous least square deconvolution and kriging using conjugate gradients, 2000.

Meyer, F. and D. Cantrell, Porous arab-d dolomite rhombs: A question of leached or arrested crystal growth, *GeoArabia, 5*, 144, 2000.

Palaz, I. And K. Marfurt, *Carbonate Seismology*, Soc. Expl. Geophys., 1997.

Pennington, W., Reservoir geophysics, *Geophys. J., 66*, 25-30, 2001.

Robertson, J. and H. Nogami, Complex seismic trace analysis of thin beds, *Geophys. J., 49*, 344-352, 1984.

Robinson, E.A. and M.T. Silvia, *Digital Signal Processing and Time Series Analysis,* Holden-Day, Inc., 1978.

Sheriff, R.E., *Reservoir Geophysics*, Soc. Expl. Geophys., 1992.

Sheriff, R.E., *Encyclopedia Dictionary of Exploration Geophysics*, Soc. Expl. Geophys, 1994.

Sheriff, R. and L. Geldart, *Exploration Seismology*, 1994.

Smith, M. and J. Scales, *Introductory Geophysical Inverse Theory*, Samizdat Press, 1997.

Taner, M., F. Koehler, and R. Sheriff, Complex seismic trace analysis, *Geophys. J., 44*, 1041-1063, 1979.

White, R.E., Properties of instantaneous seismic attributes, *The Leading Edge, 10,* 26-32, 1991.

Yilmaz, O., *Seismic Data Processing*, Soc. Expl. Geophys, 1993.